CHAPTER 3

CONSTITUTIVE MODELING OF NITINOL BEHAVIOR AND FINITE ELEMENT SIMULATIONS OF NOVEL THR IMPLANTS

This section shows a broad Finite Element (FE) model that simulates the complex thermo-mechanical behavior of shape memory alloys (nitinol alloys). At first, the one dimensional model created under the framework of Ansys Multiphysics® is depicted. The oversimplification of this model to three dimensional cases is moreover examined in this part. The finite element is utilized to gauge the performance of these newly designed THR components.

3.1 Introduction

In order to completely understand the thermo-mechanical phenomenon of nitinol in any application, developing mathematical models is inevitable. Currently, the researchers are gaining much interest in the area of constitutive modeling of shape memory alloys. The developed models are classified in two groups as: Micromechanical based models and phenomenological models (Smith, 2005).

The ***micromechanical models*** use the polycrystalline behavior of SMAs in martensite and austenite. These models develop the mathematical thermo-mechanical models in the microscopic viewpoint.

The ***phenomenological models*** assume the mixture of two solid state phases to represent the behavior of the material. Preisach models (Huo, 1989) and the irreversible thermodynamics principles (Lagoudas et al., 2007) can be listed among these models. These modeling use different energy conservation principles. Most of the parameters along

with the state variables in the phenomenological models are easy to measure. This makes these models easier to use in application and the numerical implementations.

Tanaka and Nagaki (Tanaka & Nagaki, 1982) model was among the first phenomenological models presented. Strain (ε) and temperature (T) and the martensite volume fraction which has a value between zero and one (ξ) were used as the state variables in this model. The internal variables were assumed be time and space averaged on the material domain. The model was developed by Liang and Rogers (Liang & Rogers, 1990) in later years and followed by Brinson models (Brinson, 1993) (Brinson & Huang, 1996) (Gao et al., 2007) and added the detwinned and twinned Martensite to be another internal variable for modelling the behavior according to a defined phase diagram, experimentally. It was shown that various one dimensional phenomenological models are similar but they are different in formulations of the transformation functions (Brinson & Huang, 1996). Later Gao et al. (Gao et al., 2007) improved the previous works by developing a one dimensional finite element method for truss elements, utilized to model shape memory alloys behavior in several models.

Modeling as well as the analysis of SMA beams in bending has been the focus of many investigations. Gillet et al. (Gillet et al., 1995) proposed a numerical method for predicting the phenomenon of SMA beam in case of a three-point bending test. The experiments were conducted for validating the results numerically. M. Jaber et al. (Jaber et al., 2008) used finite element analysis for predicting the SMA beam activities in a nitinol staple. The training and characterization followed by the derivation of the material properties of shape

memory alloy actuator was addressed by Hartl et al. (Hartl et al., 2010). Actuating the properties of active beam actuator and analyzing it using finite element analysis accurately was also done. A numerical tool was then developed in Abaqus (A finite element software) for simulating the thermo mechanical behavior of actuator. Tabesh et al. (Tabesh et al., 2010) made use of an assembly of combined SMA rod and tube in bending. They used the superelastic behavior of nitinol alloy and shape memory effect for designing a bi-stable actuator. The tube and rod in their actuator applied bending force due to variation in temperature in an antagonistic manner. Mineta et al. (Mineta et al., 2002) developed a micro-actuator by using a SMA bending beam. For superelastic beams, dynamic analysis was implemented by Zbiciak (Zbiciak, 2010).

Numerical techniques implemented for analyzing the SMA devices have certain limitations. Therefore, experimental validation of the results is essential. It is well-known that experiments performed using these alloys, even for carrying out simple tests, is expensive as well as difficult. Hence, there is a requirement of validating the numerical solutions against closed form solutions (Mirzaeifar et al., 2009). Exact solutions obtained computationally are less expensive and therefore they provide simulations quickly. I addition to this, exact models are more appropriate in real time simulations and to control the SMA actuators. A study to calculate the exact solution for torsional behavior of shape memory alloy bars has been conducted by Mirzaefar et al. (Mirzaeifar et al., 2009). A three dimensional model was simplified into a one-dimensional shear form. As a result, an exact method for the relationship was developed between the angular displacement and the applied torque. An analytical solution was proposed by two studies (Auricchio, 1997) for

solving the moment developed as a result of stress distribution in a superelastic material versus the curvature of a SMA Euler- Bernoulli beam. Assuming equal elastic moduli for martensite and austenite phases of the material imposes certain limitation to these solutions. Assuming equal final and initial stresses for the values of phase transformation is another limitation. Thus, this assumption is not actually what we desire in SMA specimens for tensile tests.

A well-known phenomenological constitutive models of nitinol that were used in this work will be described in the next section. The numerical implementation of the model in Ansys parametric design language (APDL) as the finite element software is also described.

The performance of the novel THR components is estimated by a developed model illustrating of the applications of novel SM and PE properties for orthopedics.

Inelastic constitutive model for nitinol

For characterizing the behavior of nitinol, the Tanaka model presented in the previous section was improved. The temperature and stress are considered as field variables in the model and independent internal variable are the single variant martensite fraction in the material. Transformation in Martensite can be triggered with either application of stress or change of temperature. As a result, the fraction of Martensite gets divided into temperature-induced and stress-induced Martensite. The twinned or temperature induced Martensite, ζ_d, comprises of a combination of self-accommodated Martensitic variants. Conversely, the stress induced Martensite, ζ_s, signifies the amount of material transformation into a

single Martensitic variant in accordance with the direction of loading. As the result of this applied stress, the austenitic NiTi lattice containing each of the 6 face-diagonal planes can shear in 2 directions and shift in 2 directions that contain 24 possible Martensite variants in 3D. The upper and lower layers during beam bending (the approximation for this application) undergo stresses in two opposite directions. The stress induced Martensite is correspondingly divided into two variables for capturing the Martensite variants that correspond to stress in positive and negative directions. Also, a stress-temperature phase transformation diagram developed empirically was used to differentiate between the transformation and non- transformation paths and regions. Laws of cosine transformation kinetics in the rate form were considered to describe the development of the temperature-induced as well as the negative and positive stress-induced Martensite fractions. As a result of this distinction, the model can predict the shape memory effect, pseudoelastic, and cyclic behavior in SMAs and dissymmetry in the tension-compression can be taken into account.

3.2 Constitutive equation

The 1D constitutive equation relating the second Piola-Kirchoff stress (S) to the thermomechanical variables Green-Lagrange strain E, volume fraction of stress induced Martensite ζ_s, and temperature T is shown:

$$S - S_0 = D(E - E_0) + \Omega\left(\zeta_S - \zeta_{S_0}\right) + \Theta(T - T_0) \qquad \text{(Eq. 1)}$$

The initial condition of that variable is denoted by the 0 subscript here. The coefficient of thermal expansion is Θ for the SMA material. D represents the modulus of SMA material

and is different for different Austenite and Martensite structures. According to the rule of mixture, it is assumed that the overall modulus of the SMA structure depends on the volumetric fraction of Martensite, ζ, (Brinson, 1993), as shown below :

$$D = D_a + \zeta(D_m - D_a) \quad \text{(Eq. 2)}$$

Where D_m and D_a are respectively the modulus value of the fully Martensitic and fully Austenitic SMA material. The transformation coefficient is Ω and is represented as:

$$\Omega = -\varepsilon_L LD \quad \text{(Eq. 3)}$$

Where: the maximum residual strain of an SMA is ε_L which is usually constant at temperatures below Austenite finish temperature, A_f. For Martensite, the volume fraction is:

$$\zeta = \zeta_d + \zeta_s \quad \text{(Eq. 4)}$$

The stress induced Martensite, ζ_s, which respectively correspond to the positive and negative directions of the applied stress is in turn decomposed into positive, ζ_{sp} ,and negative, ζ_{sn}, constituents:

$$\zeta_s = \zeta_{sp} + \zeta_{sn} \quad \text{(Eq. 5)}$$

The Tanaka-based models were obtained from the thermodynamics principles. However, they can also be represented by the micromechanics Voigt model (Brinson & Huang, 1996). This requires assuming uniform distribution of the strain over the averaged volume

element containing transformed and non-transformed material. (Quantities in bold face represent tonsorial /vector objects). The elastic E_{el}, thermalE_{th}, and transformation strain E_{tr} components are derived from Green-Lagrange strain tensor E:

$$E = E_{el} + E_{th} + E_{tr} \quad \text{(Eq. 6)}$$

The basis for large deformation is implemented here, even if switching back to small deformation is possible wherever the approximation is desired. The referential coordinates are X, Y, and Z are in the undeformed state of the material. The displacement components are taken to be u, v, and w in such a coordinate system. The deformation gradient tensor F is described as:

$$F = \begin{bmatrix} 1 + \frac{\partial u}{\partial X} & \frac{\partial u}{\partial Y} & \frac{\partial u}{\partial Z} \\ \frac{\partial v}{\partial X} & 1 + \frac{\partial v}{\partial Y} & \frac{\partial v}{\partial Z} \\ \frac{\partial w}{\partial X} & \frac{\partial w}{\partial Y} & 1 + \frac{\partial w}{\partial Z} \end{bmatrix} \quad \text{(Eq. 7)}$$

The Green-Lagrange strain, which is a measure of deformation in the material based on the square of change of length without including rigid body displacement or rotation, can be proved to be:

$$E = \frac{1}{2}(F^T.F - I) \quad \text{(Eq. 8)}$$

The second order identity tensor is denoted as "I".The infinitesimal strain tensor ε is obtained by avoiding the nonlinear elements of "E":

$$\varepsilon = \frac{1}{2}(F^T + F) - I = \begin{bmatrix} \frac{\partial u}{\partial X} & \frac{1}{2}\left(\frac{\partial u}{\partial Y} + \frac{\partial v}{\partial X}\right) & \frac{1}{2}\left(\frac{\partial u}{\partial Z} + \frac{\partial w}{\partial X}\right) \\ \frac{1}{2}\left(\frac{\partial u}{\partial Y} + \frac{\partial v}{\partial X}\right) & \frac{\partial v}{\partial Y} & \frac{1}{2}\left(\frac{\partial v}{\partial Z} + \frac{\partial w}{\partial Y}\right) \\ \frac{1}{2}\left(\frac{\partial u}{\partial Z} + \frac{\partial w}{\partial X}\right) & \frac{1}{2}\left(\frac{\partial v}{\partial Z} + \frac{\partial w}{\partial Y}\right) & \frac{\partial w}{\partial Z} \end{bmatrix} \quad \text{(Eq. 9)}$$

The Cauchy stress tensor $\boldsymbol{\sigma}$ is basically defined as the force per unit of the deformed area. The strain measure is the small deformation strain tensor $\boldsymbol{\varepsilon}$ that is appropriate to use with the Cauchy stress tensor σ. The problem with using the Cauchy stress tensor for analyzing materials experiencing large deformation is that the area in the deformed configuration is unknown. Therefore, a need for a stress measure arises which can be used in the reference or undeformed pattern. The 2nd Piola-Kirchoff stress tensor S is described as the force mapped to the undeformed configuration per unit of the undeformed area. S is symmetric and energetically consistent with Green-Lagrange strain E. In other words, elastic strain energy density which is calculated with the 2nd Piola-Kirchoff stress tensor using the Green-Lagrange strain will be the similar to that calculated with the Cauchy stress tensor and small deformation strain tensor:

$$\sigma : \varepsilon = S : E \quad \text{(Eq. 10)}$$

The elastic stress-strain relationship denotes that:

$$S = C : (E - E_{th} - E_{tr}) \quad \text{(Eq. 11)}$$

C is the elastic stiffness tensor and is defined as before by the rule of mixture:

$$C = C_A + \zeta(C_M - C_A) \quad \text{(Eq. 12)}$$

The thermal strain is not included in this study due to its insignificance as compared to transformation strain.

2nd Piola-Kirchoff (PK) stress has the following relationship with the Cauchy stress:

$$S = JF^{-1}.\sigma.F^{-1}, \sigma = J^{-1}F.S.F^{T}, J = det(F) \quad \text{(Eq. 13)}$$

Objective of virtual work in the quasi-static form (neglecting the inertial terms) is used for solving the stress/strain state of the material. The correlation between the variation of the strain $\boldsymbol{\delta E}$, 2nd PK stress $\boldsymbol{S}$ in the undeformed (reference) body $\boldsymbol{V_0}$, the variation of the displacement field $\boldsymbol{\delta u}$, density of the external body forces per unit mass $\boldsymbol{f}$, and the field of tractions **T** (stress vectors) acting upon the deformed surface S (stress boundary condition) can be formulated as (Bower, 2009):

$$\int_{V_0} S{:}\,\delta E \; dV_0 = \int_{V_0} \rho_0 f.\delta u \; dV_0 + \int_S T.\delta u ds \quad \text{(Eq. 14)}$$

Where ρ_0 is the material density in the undeformed state. For small deformation condition equation 14 is presented as:

$$\int_V \sigma{:}\,\delta\varepsilon \; dv = \int_v \rho f.\delta u \; dV + \int_S T.\delta u ds \quad \text{(Eq. 15)}$$

Here V and ρ correspond to the deformed body.

3.2.1 Transformation kinetics law

an empirically-derived cosine model is used to obtain the transformation stresses and transformation equations for defining the relationship between the Martensite fraction, temperature and stress, during the transformation. They must be reformed to include the stress induced Martensite decomposition into positive and negative portions. The SMA kinetics law described is based on loading path on a Cauchy stress-temperature phase diagram as shown in Figure 3.1. Both, the current position on the meta-equilibrium ($\sigma - T$) phase diagram and the history of the thermomechanical loading are obtained from the fraction of Martensite. The compression part of the diagram can approximately be similar to the tensile part in the opposite direction (Bekker & Brinson, 1997). However, modification in the critical values of stress can be possible for starting the transformation or the slopes of the transformation bands in accordance with findings from thermomechanical experiments on the material. Various researchers have proposed modifications (not included here) in this diagram such as distinction between transformation from twinned Martensite to Austenite than from detwinned Martensite to Austenite (Popov & Lagoudas, 2007) or linear increase in the critical values of the stress required for detwinning in the temperatures below M_S.

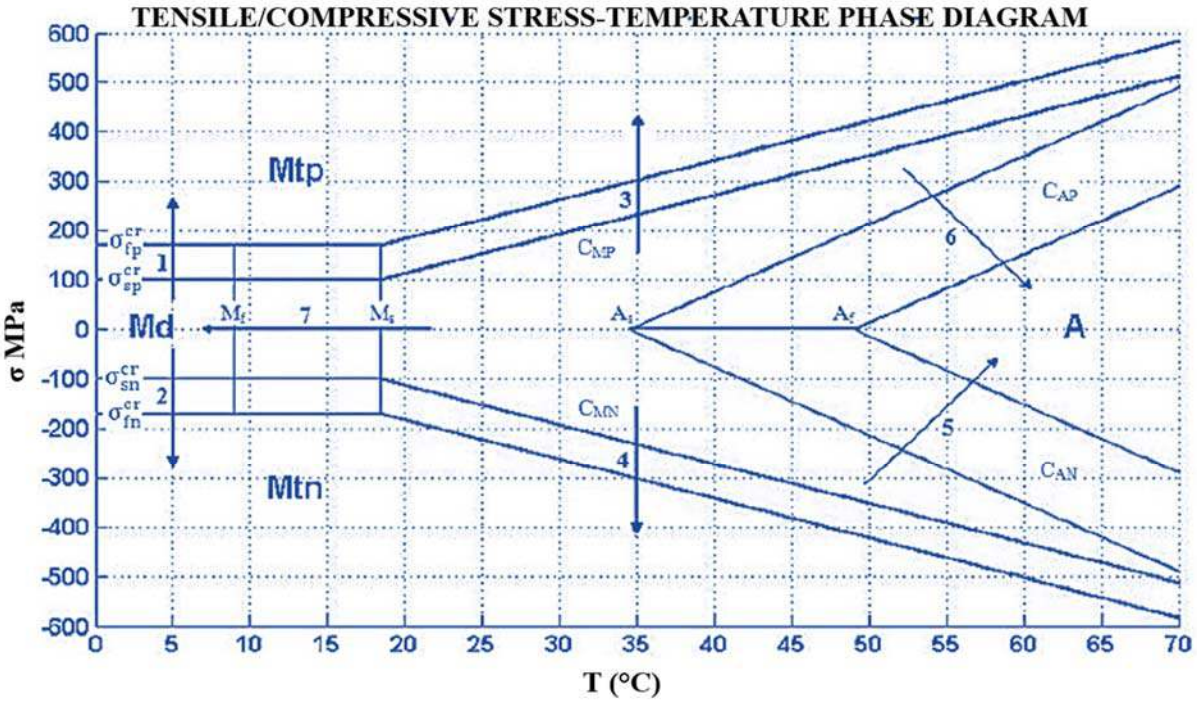

Figure 3.1: Empirical stress-temperature phase diagram showing different paths of transformation; detwinned Martensite M_d, twinned Martensite in the positive M_{tp} and negative M_{tn} directions, and Austenite A.

Figure 3.1 shows that the diagram is divided into transformation regions above which the transformation to the corresponding phase occurs. In this figure, M_S, M_f, A_S, and A_f, denote Martensite start and finish transformation temperatures and Austenite start and finish transformation temperatures, respectively. Additionally, σ_s^{cr} and σ_f^{cr} are critical stresses for the start and finish of the transformation into stress-induced Martensite in temperature ranges below M_S.

The critical stress value at the start and end of the transformation is effectively stated as a linear function of temperature (according to Clausius- Clapeyron relation assuming

equal stiffness and thermal expansion coefficient for Martensite and Austenite) with a slope of C_M for Martensite and C_A for Austenite transformation (Brinson, 1993). The stress influence factors can be different for the positive, C_{MP} & C_{AP}, and negative, C_{MN} & C_{AN} directions.

The stress-temperature paths signify the transformations as: (Paths 1 and 3 in Figure 3.1), in the positive direction, the forward transformation to twinned Martensite M_{tp}:

$$\{1\}: \text{if } T < M_S; \qquad \sigma_{sp}^{cr} < \sigma < \sigma_{fp}^{cr}, \text{ and } \dot{\sigma} > 0 \qquad \text{(Eq. 16)}$$

$$\zeta_{sp} = \frac{1-\zeta_{sp_0}}{2}\cos\left\{\frac{\pi}{\sigma_{sp}^{cr}-\sigma_{fp}^{cr}}\left[\sigma - \sigma_{fp}^{cr}\right]\right\} + \frac{1+\zeta_{sp_0}}{2}$$

$$\zeta_d = \zeta_{d_0}\left(\frac{1-\zeta_{sp}}{1-\zeta_{sp_0}}\right),\ \zeta_{sn} = \zeta_{sn_0}\left(\frac{1-\zeta_{sp}}{1-\zeta_{sp_0}}\right),\ \zeta_s = \zeta_{sp} + \zeta_{sn}$$

$$\{3\}: \text{if } T > M_S, \qquad \text{(Eq. 17)}$$

$$\sigma_{sp}^{cr} + C_{MP}(T - M_s) < \sigma < \sigma_{fp}^{cr} + C_{MP}(T - M_s), and\ \dot{\sigma} > TC_{MP}$$

$$\zeta_{sp} = \frac{1-\zeta_{sp_0}}{2}\cos\left\{\frac{\pi}{\sigma_{sp}^{cr}-\sigma_{fp}^{cr}}\left[\sigma - \sigma_{fp}^{cr} - C_{M_p}(T - M_S)\right]\right\} + \frac{1+\zeta_{sp_0}}{2}$$

$$\zeta_d = \zeta_{d_0}\left(\frac{1-\zeta_{sp}}{1-\zeta_{sp_0}}\right),\ \zeta_{sn} = \zeta_{sn_0}\left(\frac{1-\zeta_{sp}}{1-\zeta_{sp_0}}\right),\ \zeta_s = \zeta_{sp} + \zeta_{sn}$$

The reason behind the third condition for the above equations can be clarified by referring to Figure 3.2. The trajectory of the state of stress and temperature on the stress-temperature phase diagram should be appropriate for the transformation to take place. The transformation to twinned Martensite occurs only if the rate of change for the stress

and temperature follows the circle-dotted line which means if $\dot{\sigma} > \dot{T}C_{MP}$. By the same token, the reverse transformation to Austenite happens on the square-dotted line i.e. only if $\dot{\sigma} < \dot{T}C_{MP}$.

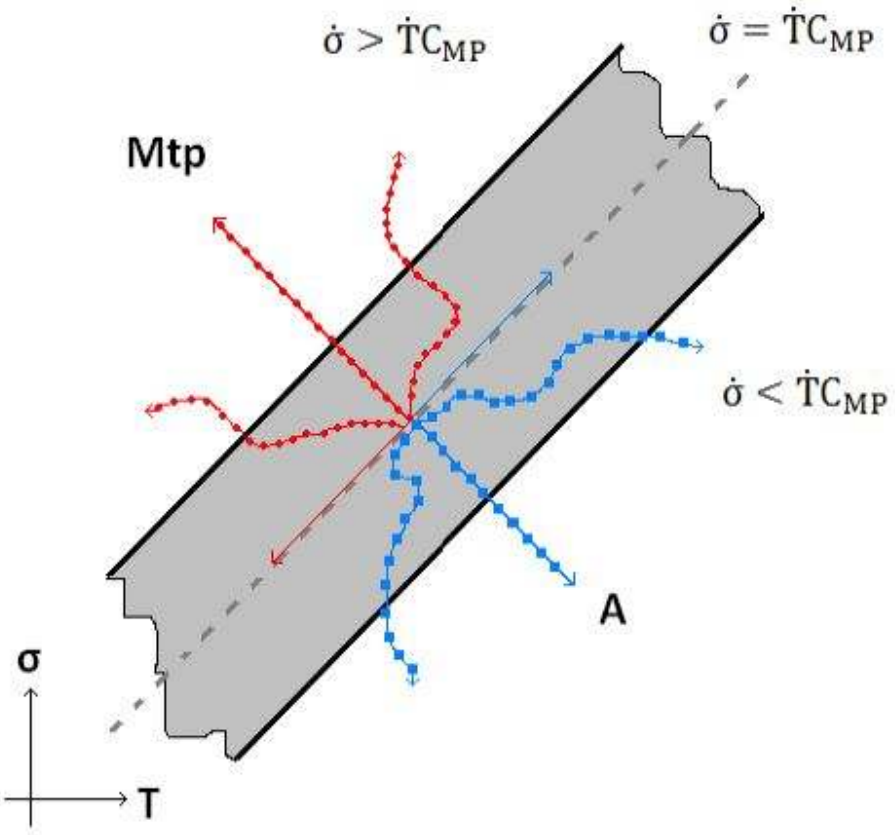

Figure 3.2: The path conditions for transformation to Martensite or Austenite.

(Paths 2 and 4 in Figure 1), in the negative direction, forward transformation to twinned Martensite M_{tn}:

$$\{2\}: \text{if } T < M_S, \text{ and } \sigma_{fp}^{cr} < \sigma < \sigma_{sn}^{cr}, \text{ and } \dot{\sigma} < 0 \qquad \text{(Eq. 18)}$$

$$\zeta_{sn} = \frac{1-\zeta_{sn_0}}{2}\cos\left\{\frac{\pi}{\sigma_{sn}^{cr}-\sigma_{fn}^{cr}}\left[\sigma-\sigma_{fn}^{cr}\right]\right\}+\frac{1+\zeta_{sn_0}}{2}$$

$$\zeta_d = \zeta_{d_0}\left(\frac{1-\zeta_{sn}}{1-\zeta_{sn_0}}\right), \zeta_{sp} = \zeta_{sp_0}\left(\frac{1-\zeta_{sn}}{1-\zeta_{sn_0}}\right), \zeta_s = \zeta_{sp} + \zeta_{sn}$$

$\{4\}$: if $T > M_S$, and (Eq. 19)

$$\sigma_{fn}^{cr} + C_{Mn}(T - M_s) < \sigma < \sigma_{sn}^{cr} + C_{Mn}(T - M_s), and\ \dot{\sigma} > TC_{Mn}$$

$$\zeta_{sn} = \frac{1-\zeta_{sn_0}}{2}\cos\left\{\frac{\pi}{\sigma_{sn}^{cr}-\sigma_{fn}^{cr}}\left[\sigma - \sigma_{fn}^{cr} - C_{M_n}(T - M_S)\right]\right\} + \frac{1+\zeta_{sn_0}}{2}$$

$$\zeta_d = \zeta_{d_0}\left(\frac{1-\zeta_{sn}}{1-\zeta_{sn_0}}\right), \zeta_{sp} = \zeta_{sp_0}\left(\frac{1-\zeta_{sn}}{1-\zeta_{sn_0}}\right), \zeta_s = \zeta_{sp} + \zeta_{sn}$$

(Paths 5 and 6 in Figure 3.1) Reverse transformation to Austenite:

$\{5\}$: if $T > A_S$, and (Eq. 20)

$$C_{An}(T - A_s) < \sigma < min\left[0, C_{An}\left(T - A_f\right)\right], and\ \dot{\sigma} > \dot{T}C_{An}$$

$$\zeta_{sp} = \frac{\zeta_{sp_0}}{2}\left\{\cos\left[a_A\left(T - A_s - \frac{\sigma}{C_{An}}\right)\right] + 1\right\}$$

$$\zeta_{sn} = \frac{\zeta_{sn_0}}{2}\left\{\cos\left[a_A\left(T - A_s - \frac{\sigma}{C_{An}}\right)\right] + 1\right\}$$

$$\zeta_d = \frac{\zeta_{d_0}}{2}\left\{\cos\left[a_A\left(T - A_s - \frac{\sigma}{C_{An}}\right)\right] + 1\right\}$$

$$\zeta = \zeta_d + \zeta_{sp} + \zeta_{sn}$$

$\{6\}$: if $T > A_S$, and (Eq. 21)

$$max\left[0, C_{Ap}\left(T - A_f\right)\right] < \sigma < C_{Ap}(T - A_s), and\ \dot{\sigma} > \dot{T}C_{Ap}$$

$$\zeta_{sp} = \frac{\zeta_{sp_0}}{2}\left\{\cos\left[a_A\left(T - A_s - \frac{\sigma}{C_{Ap}}\right)\right] + 1\right\}$$

$$\zeta_{sn} = \frac{\zeta_{sn_0}}{2}\left\{\cos\left[a_A\left(T - A_s - \frac{\sigma}{C_{Ap}}\right)\right] + 1\right\}$$

$$\zeta_d = \frac{\zeta_{t_0}}{2}\left\{\cos\left[a_A\left(T - A_s - \frac{\sigma}{C_{Ap}}\right)\right] + 1\right\}$$

$$\zeta = \zeta_d + \zeta_{sp} + \zeta_{sn}$$

(Path 7 in Figure 3.1) Forward Transformation to twinned Martensite M_d:

$$\{7\} \text{ if } M_f < T < M_S, \text{ and } \sigma_{fn}^{cr} < \sigma < \sigma_{fp}^{cr}, \text{ and } \dot{T} < 0 \qquad \text{(Eq. 22)}$$

$$\zeta_d = \frac{\left(1 - \zeta_{sp} - \zeta_{sn}\right) - \zeta_{d_0}}{2}\left\{\cos\left[a_M(T - M_f)\right]\right\}$$

$$+ \frac{\left(1 - \zeta_{sp} - \zeta_{sn}\right) + \zeta_{d_0}}{2}$$

$$\zeta = \zeta_d + \zeta_{sp} + \zeta_{sn}$$

In the above equations, the rate of change of stress is $\dot{\sigma}$ and $\dot{T}$ is the temperature; also $a_m = \frac{\pi}{M_s - M_f}$, and $a_A = \frac{\pi}{A_f - A_s}$.

The same argument, can be set forth regarding the path conditions for the rest of the transformation equations. For the transformation to occur. the direction of the thermomechanical loading path is essential and should be such that its normal distance to the destination phase boundary reduces continuously.

Moreover, the zero value for different variables (e.g. ζ_{sp_0}) are noted as the amount of that variable at the start (or re-start) of the transformation process.

Initial or 0 values are described according to the following equations:

$$\{1\}\ \zeta_{sp_0} = \frac{2\zeta_{sp} - 1 - \cos\left\{\frac{\pi}{\sigma_{sp}^{cr} - \sigma_{fp}^{cr}}\left[\sigma - \sigma_{fp}^{cr}\right]\right\}}{1 - \cos\left\{\frac{\pi}{\sigma_{sp}^{cr} - \sigma_{fp}^{cr}}\left[\sigma - \sigma_{fp}^{cr}\right]\right\}}$$

$$\zeta_{sn_0} = \zeta_{sn}\left(\frac{1-\zeta_{sp_0}}{1-\zeta_{sp}}\right),\ \zeta_{d_0} = \zeta_d \frac{1-\zeta_{sp_0}}{1-\zeta_{sp}}$$

$$\{2\}\ \ \zeta_{sn_0} = \frac{2\zeta_{sn} - 1 - \cos\left\{\frac{\pi}{\sigma_{sn}^{cr} - \sigma_{fn}^{cr}}\left[\sigma - \sigma_{fn}^{cr}\right]\right\}}{1 - \cos\left\{\frac{\pi}{\sigma_{sn}^{cr} - \sigma_{fn}^{cr}}\left[\sigma - \sigma_{fn}^{cr}\right]\right\}},$$

$$\zeta_{sp_0} = \zeta_{sp}\left(\frac{1-\zeta_{sn_0}}{1-\zeta_{sn}}\right),\ \zeta_{d_0} = \zeta_d \frac{1-\zeta_{sn_0}}{1-\zeta_{sn}}$$

$$\{3\}\ \ \zeta_{sp_0} = \frac{2\zeta_{sp} - 1 - \cos\left\{\frac{\pi}{\sigma_{sp}^{cr} - \sigma_{fp}^{cr}}\left[\sigma - \sigma_{fp}^{cr} - C_{Mp}(T - M_s)\right]\right\}}{1 - \cos\left\{\frac{\pi}{\sigma_{sp}^{cr} - \sigma_{fp}^{cr}}\left[\sigma - \sigma_{fp}^{cr} - C_{Mp}(T - M_s)\right]\right\}}$$

$$\zeta_{sn_0} = \zeta_{sn}\left(\frac{1-\zeta_{sp_0}}{1-\zeta_{sp}}\right),\ \zeta_{d_0} = \zeta_d \frac{1-\zeta_{sp_0}}{1-\zeta_{sp}}$$

$$\{4\}\ \zeta_{sn_0} = \frac{2\zeta_{sn} - 1 - \cos\left\{\frac{\pi}{\sigma_{sn}^{cr} - \sigma_{fn}^{cr}}\left[\sigma - \sigma_{fn}^{cr} - C_{Mn}(T - M_s)\right]\right\}}{1 - \cos\left\{\frac{\pi}{\sigma_{sn}^{cr} - \sigma_{fn}^{cr}}\left[\sigma - \sigma_{fn}^{cr} - C_{Mn}(T - M_s)\right]\right\}}$$

$$\zeta_{sp_0} = \zeta_{sp}\left(\frac{1-\zeta_{sn_0}}{1-\zeta_{sn}}\right),\ \zeta_{d_0} = \zeta_d \frac{1-\zeta_{sn_0}}{1-\zeta_{sn}}$$

$$\{5\} \quad \zeta_{sp_0} = \frac{2\zeta_{sp}}{\left\{\cos\left[a_A\left(T-A_s-\frac{\sigma}{C_{An}}\right)\right]+1\right\}},$$

$$\zeta_{sn_0} = \frac{2\zeta_{sn}}{\left\{\cos\left[a_A\left(T-A_s-\frac{\sigma}{C_{An}}\right)\right]+1\right\}},$$

$$\zeta_{d_0} = \frac{2\zeta_d}{\left\{\cos\left[a_A\left(T-A_s-\frac{\sigma}{C_{An}}\right)\right]+1\right\}}$$

$$\{6\} \quad \zeta_{sp_0} = \frac{2\zeta_{sp}}{\left\{\cos\left[a_A\left(T-A_s-\frac{\sigma}{C_{Ap}}\right)\right]+1\right\}},$$

$$\zeta_{sn_0} = \frac{2\zeta_{sn}}{\left\{\cos\left[a_A\left(T-A_s-\frac{\sigma}{C_{Ap}}\right)\right]+1\right\}},$$

$$\zeta_{d_0} = \frac{2\zeta_d}{\left\{\cos\left[a_A\left(T-A_s-\frac{\sigma}{C_{Ap}}\right)\right]+1\right\}}$$

$$\{7\} \quad \zeta_{d_0} = \frac{2\zeta_d-(1-\zeta_{sp}-\zeta_{sn})\{1+\cos[a_M(T-M_f)]\}}{\{1-\cos[a_M(T-M_f)]\}}$$

There is a problem of division by zero in the initial condition equations. It was circumvented by substituting the Taylor series expansion (about zero) of the trigonometric functions in such cases.

Transformation kinetics relations for the above mentioned thermomechanical pats is as follows:

$$\dot{\zeta} = \left[\dot{\zeta_{sp}}\dot{\zeta_{sn}}\dot{\zeta_d}\right]^T = A.C^d \text{ or } \zeta_i = A_{ij}C_j^d \quad \text{(Eq. 23)}$$

Change of rate for different martensite phases w.r.t. the pseudo time is embedded in matrix A and is expressed as:

$$A_{11} = \frac{1-\zeta_{sp_0}}{2}\left(\frac{-\pi\dot{\sigma}}{\sigma_{sp}^{cr}-\sigma_{fp}^{cr}}\right)\sin\left\{\frac{\pi}{\sigma_{sp}^{cr}-\sigma_{fp}^{cr}}\left(\sigma-\sigma_{fp}^{cr}\right)\right\},$$

$$A_{21} = \zeta_{sn_0}\frac{-A_{11}}{1-\zeta_{sp_0}},\ A_{31} = \zeta_{d_0}\frac{-A_{11}}{1-\zeta_{sp_0}};$$

$$A_{12} = \zeta_{sp_0}\frac{-A_{22}}{1-\zeta_{sn_0}},$$

$$A_{13} = \frac{1-\zeta_{sp_0}}{2}\left(\frac{-\pi\left(\dot{\sigma}-C_{Mp}\dot{T}\right)}{\sigma_{sp}^{cr}-\sigma_{fp}^{cr}}\right)\sin\left\{\frac{\pi}{\sigma_{sp}^{cr}-\sigma_{fp}^{cr}}\left[\sigma-\sigma_{fp}^{cr}-C_{Mp}(T-M_s)\right]\right\},$$

$$A_{23} = \zeta_{sn_0}\frac{-A_{13}}{1-\zeta_{sp_0}},$$

$$A_{33} = \zeta_{d_0}\frac{-A_{13}}{1-\zeta_{sp_0}}$$

$$A_{14} = \zeta_{sp_0}\frac{-A_{24}}{1-\zeta_{sn_0}},$$

$$A_{24} = \frac{1-\zeta_{sn_0}}{2}\left(\frac{-\pi(\dot{\sigma}-C_{Mn}\dot{T})}{\sigma_{sn}^{cr}-\sigma_{fn}^{cr}}\right)\sin\left\{\frac{\pi}{\sigma_{sn}^{cr}-\sigma_{fn}^{cr}}\left[\sigma-\sigma_{fn}^{cr}-C_{Mn}(T-M_s)\right]\right\},$$

$$A_{34} = \zeta_{d_0} \frac{-A_{24}}{1-\zeta_{sn_0}};$$

$$A_{15} = -\frac{a_A}{2}\zeta_{sp_0}\left(\dot{T} - \frac{\dot{\zeta}}{C_{An}}\right)\sin\left\{a_A\left(T - A_S - \frac{\sigma}{C_{An}}\right)\right\},$$

$$A_{25} = -\frac{a_A}{2}\zeta_{sn_0}\left(\dot{T} - \frac{\dot{\zeta}}{C_{An}}\right)\sin\left\{a_A\left(T - A_S - \frac{\sigma}{C_{An}}\right)\right\},$$

$$A_{35} = -\frac{a_A}{2}\zeta_{d_0}\left(\dot{T} - \frac{\dot{\sigma}}{C_{An}}\right)\sin\left\{a_A\left(T - A_S - \frac{\sigma}{C_{An}}\right)\right\},$$

$$A_{16} = -\frac{a_A}{2}\zeta_{sp_0}\left(\dot{T} - \frac{\dot{\sigma}}{C_{Ap}}\right)\sin\left\{a_A\left(T - A_S - \frac{\sigma}{C_{Ap}}\right)\right\},$$

$$A_{26} = -\frac{a_A}{2}\zeta_{sn_0}\left(\dot{T} - \frac{\dot{\sigma}}{C_{Ap}}\right)\sin\left\{a_A\left(T - A_S - \frac{\sigma}{C_{Ap}}\right)\right\},$$

$$A_{36} = -\frac{a_A}{2}\zeta_{d_0}\left(\dot{T} - \frac{\dot{\sigma}}{C_{Ap}}\right)\sin\left\{a_A\left(T - A_S - \frac{\sigma}{C_{Ap}}\right)\right\};$$

$$A_{17} = A_{27} = 0,$$

$$A_{37} = -a_M \frac{(1-\zeta_{sp}-\zeta_{sn})-\zeta_{d_0}}{2}\dot{T}\sin\{a_M(T - M_f)\} - \frac{(\zeta_{sp}+\zeta_{sn})}{2}(1 + \cos\{a_M(T - M_f)\})$$

The conditions of transformation for each path is described by vector C^d. It confirms that no transformation takes place while loading along the dead directions or acting in the dead zones. It can be expressed as:

$$C_1^d = \langle T < M_s\rangle * \langle \sigma < \sigma_{fp}^{cr}\rangle * \langle \sigma_{sp}^{cr} < \sigma\rangle * \langle 0 < \dot{\sigma}\rangle,$$

$$C_2^d = \langle T < M_s \rangle * \langle \sigma < \sigma_{sn}^{cr} \rangle * \langle \sigma_{fn}^{cr} < \sigma \rangle * \langle \dot{\sigma} < 0 \rangle,$$

$$C_3^d = \langle M_s \leq T \rangle * \langle \sigma < \sigma_{fp}^{cr} + C_{Mp}(T - M_s) \rangle * \langle \sigma_{sp}^{cr} + C_{Mp}(T - M_s) < \sigma \rangle * \langle C_{Mp}\dot{T} < \dot{\sigma} \rangle,$$

$$C_4^d = \langle M_s \leq T \rangle * \langle \sigma < \sigma_{sn}^{cr} + C_{Mn}(T - M_s) \rangle * \langle \sigma_{fn}^{cr} + C_{Mn}(T - M_s) < \sigma \rangle * \langle \dot{\sigma} < C_{Mn}\dot{T} \rangle,$$

$$C_5^d = \langle A_s \leq T \rangle * \langle \sigma < min\left[0, C_{An}\left(T - A_f\right)\right] \rangle * \langle C_{An}(T - A_s) < \sigma \rangle * \langle C_{An}\dot{T} < \dot{\sigma} \rangle,$$

$$C_6^d = \langle A_s \leq T \rangle * \langle \sigma < C_{Ap}(T - A_s) \rangle * \langle Max\left[0, C_{Ap}\left(T - A_f\right)\right] < \sigma \rangle * \langle \dot{\sigma} < C_{Ap}\dot{T} \rangle,$$

$$C_7^d = \langle T < M_s \rangle * \langle M_f \leq T \rangle * \langle \sigma < \sigma_{fp}^{cr} \rangle * \langle \sigma_{fn}^{cr} < \sigma \rangle * \langle \dot{T} < 0 \rangle$$

The quantity $\langle * \rangle$ is equal to one if logical expression inside it is valid; otherwise it is zero.

In this study, only 1D and cantilever bending situations are examined and components of transformation strain apart from axial (z direction) are ignored. Therefore, there will be:

$$E_{ZZ}^{tr} = \varepsilon_{Lp}\zeta_{sp} + \varepsilon_{Ln}\zeta_{sn} \qquad \text{(Eq. 26)}$$

ε_{Lp} and ε_{Ln} are the maximum transformation strains in tension and compression respectively. The coefficient of asymmetry η is defined as the following proportionalities:

$$\tau = -\frac{C_{An}}{C_{Ap}} = -\frac{C_{Mn}}{C_{Mp}} = -\frac{\sigma_{sn}^{cr}}{\sigma_{sp}^{cr}} = -\frac{\sigma_{fn}^{cr}}{\sigma_{fp}^{cr}} = -\frac{\varepsilon_{Lp}}{\varepsilon_{Ln}} \qquad \text{(Eq. 27)}$$

Although asymmetric properties in tension and compression (Vacher & Laxcellent, 1991) (Orgeas & Favier, 1995) (Gall et al., 1999) are shown by nitinol, the properties of

transformation in compression are considered to be opposite (unless otherwise stated) of their tensional counterparts; i.e. $\tau = 1$.

3.3 Numerical implementation of the constitutive model in ANSYS Multiphysics®

The described constitutive model for prediction of the phenomenon of shape memory alloy materials cannot be used to model various geometries and conditions without implementation into a numerical environment. To be able to have the capability of analyzing complex problems, a developed code into the Ansys finite Framework (ANSYS® Academic Research) as a Mechanical APDL Command is used. This code is the numerically implements the defined constitutive model. The method in which the global APDL solver uses the command line to model a nonlinear material like shape memory alloys. As shown, the model uses displacement based finite element analysis, which is known as the more popular method. Based on the thermo-mechanical loading pass, solver begins by guessing the appropriate initial deformation over the domain nodes by solving the linear problem (elastic stiffness matrix). These strains are fed into the command. The algorithm updates the stresses based on the shape memory alloys constitutive model. Other than the updated stresses, the local tangent stiffness over the material point domain is also calculated. These stresses are used to calculate the forces on the elements by integration over the element. The resultant force applied on all nodes is calculated which needs to be zero to satisfy the static equilibrium. The residual forces on these nodes are calculated and if the magnitude is less than a certain tolerance the solution is valid and the solver moves forward to the next loading path. If the magnitude is large,

Full Newton-Raphson method is used to guess new values for the deformations where the calculated tangent stiffness in the program relates the residual force to the new guessed displacements.

Inside the previously developed Ansys APDL program, as described before, for each node the strain is the input from the Ansys global solver and the stress and the stress tangent stiffness are the outputs. The APDL algorithm assumes no transformation at the start of each step. Thus, if with the elastic assumption, happens then the UMAT can return the result as the stress of the node. But if violation of the inequality happens with the elastic assumption, it means that transformation is taking place. Using the return mapping algorithm, the required stress and tangent stiffness can be found in the transformation condition. In this case, the increment of the martensite volume fraction evolves and based on the described constitutive equations the resultant stress is calculated. Each time the transformation function is recalculated and once condition is achieved the results will be returned to the global solver.

3.4 Results and Discussions

3.4.1 Preliminary Simulations

Now that we have the numerical tool implemented into the Ansys solver to analyze shape memory alloys behavior, we are able to observe the results for some preliminary tests. These two preliminary simulations were conducted to observe the specific thermo-mechanical behaviors of shape memory alloys in tension.

In the following sections, a block out of shape memory alloy material of 10 mm length with material properties reported in Table 3.1 is used for the simulations. The block model is made in Creo Parametric 3D modeling software (PTC, Inc., Massachusetts, USA), GUI as presented in Figure 3.3. This model has been imported in Ansys APDL platform via CAD configuration manager. The left side nodes and bottom face of the block are constrained and uniaxial load with tensile stress of $\sigma = 600\,MPa$ is applied on the top face equal forces are applied to the right end nodes.

Table 3.1: Material properties of shape memory alloy used in preliminary simulations for superelastic test case

Shape memory alloy Constants	Abbreviation	Value
Starting stress value for the forward phase transformation	σ_s^{AS}	520 MPa
Final stress value for the forward phase transformation	σ_f^{AS}	600 MPa
Starting stress value for the reverse phase transformation	σ_s^{SA}	300 MPa
Final stress value for the reverse phase transformation	σ_f^{SA}	200 MPa
Maximum residual strain	$\overline{\varepsilon_L}$	0.07
Parameter measuring the difference between material response in tension and compression	α	0
Material Properties	**Abbreviation**	**Value**
Elastic modulus (Austenite phase)	E_A	60×10^3 MPa
Poisson Ratio	μ	0.3

3.4.2 Simulation of a superelastic case

In the first simulation, we want to observe the superelasticity behavior of the material in tension. For this reason, the temperature of the block is set to 259.15 K to be above the austenite final temperature (A_f). The resulted stress against strain on the simulation due to the applied force is plotted.

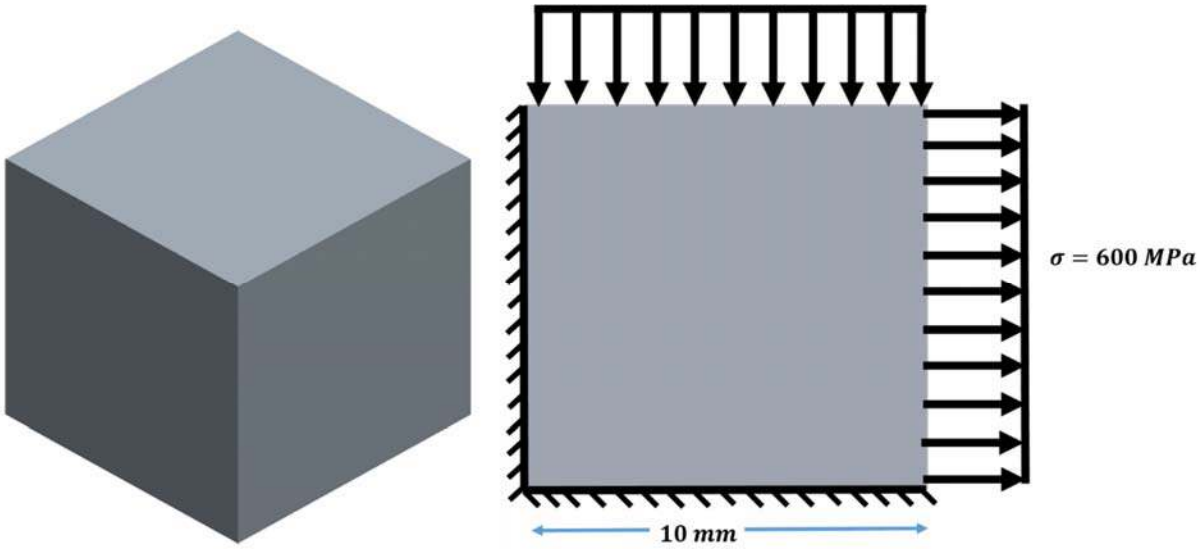

Figure 3.3: Prepared block in Creo parametric (PTC, Inc., Massachusetts, USA) for preliminary solution (Left), illustration of boundary conditions (Right)

3.4.3 Preliminary simulation for 2D uniaxial tension load

In this test case element type PLANE182 is chosen for 2D simulation of this above mentioned block. This element is a plane element or an axisymmetric element. Four nodes with two degree of freedom at each node defines this: translation in the nodal X and Y directions (Figure 3.4). Hyperelasticity, plasticity, stress stiffening, large strain

capabilities, and large deflection are present in the element. It is also mixed formulation capability for simulation deformations of nearly incompressible elastoplastic materials, and fully incompressible hyperelastic materials. This element is best suited for analyzing 2D superelastic case of shape memory alloys. Meshed model is presented in figure 3.5.

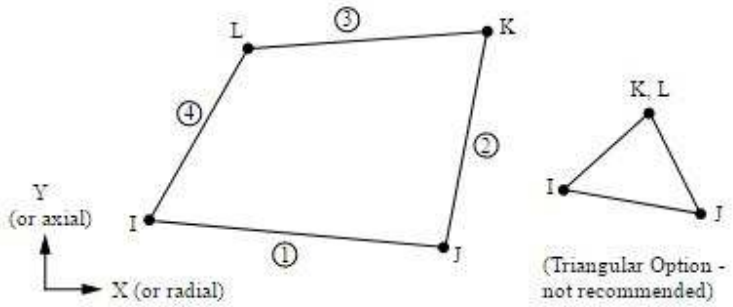

Figure 3.4: Schematic illustration of element type (PLANE 182)

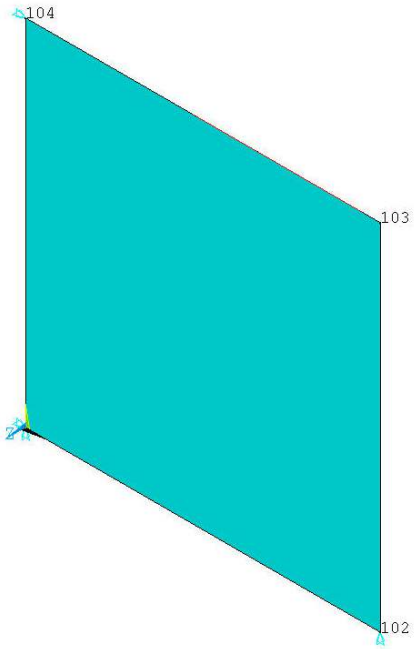

Figure 3.5: Meshed plane in Ansys for preliminary analysis (Element size=10 mm)

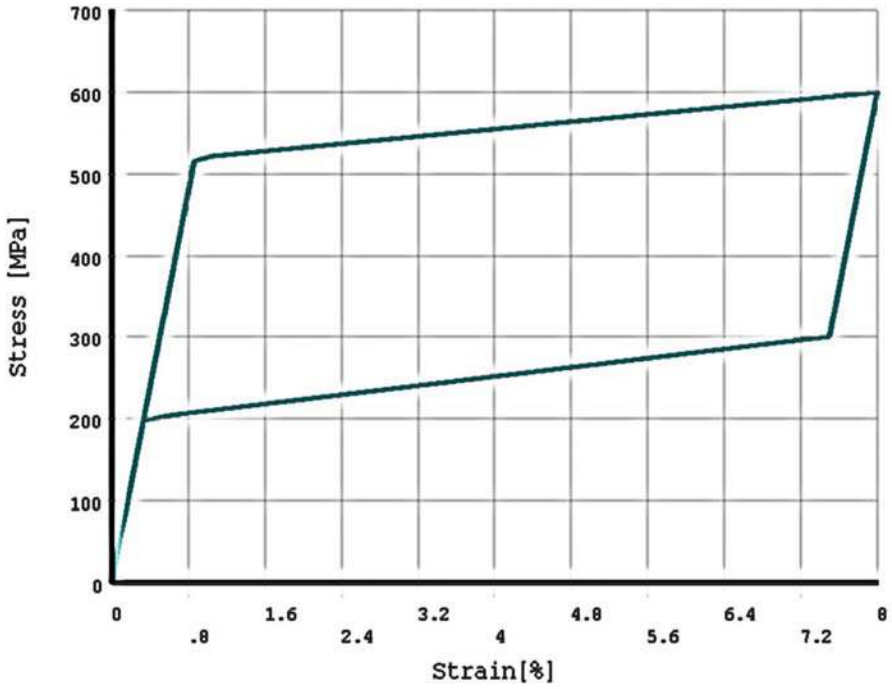

Figure 3.6: Preliminary output of simulation of superelastic behavior of Nitinol

The resulted stress against strain on the block due to the applied force for 2D case is designed in Figure 3.6. The generated strain due to transformation in loading is fully recovered in the unloading path as described. This simulation showed the ability of the numerical tool in modeling the superelasticity of thermo mechanical behavior for shape memory alloys. The corresponding Ansys script for the simulation of 2D uniaxial tension load is listed in Appendix.

3.4.4 Preliminary simulation for 3D uniaxial tension load

The developed constitutive equations are verified by uniaxial tension load of block as discussed above. The meshing of this block is shown in figure 3.7.

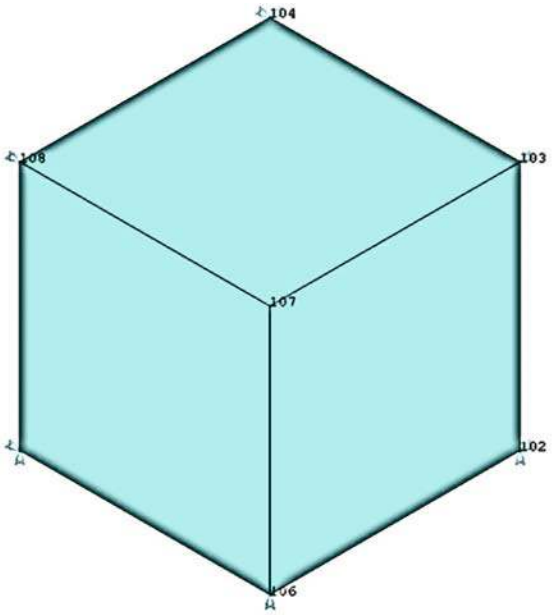

Figure 3.7: Meshed plane in Ansys for preliminary analysis

Material properties are applied and loading condition are given; result of stress versus strain is plotted which is similar as shown in figure 6 for plane test case. These simulation shows the ability of numerical tool to model the complex designs made from nitinol alloys. The corresponding Ansys script for the simulation of 3D uniaxial tension load is listed in Appendix.

3.4.5 Simulation of a shape memory case

To simulate the shape memory effect, the temperature of the block needs to be below the austenite start temperature. To this end, the temperature is set to 253.15 K and the initial state is in austenite phase. One cycle of uniaxial displacement loading of 0.35 mm is applied in vertical direction. The whole process includes tension, unload, compression, and unload. The temperature is then increased to 285.15 K, which is above the austenite finish temperature. In this test element SOLID185 homogeneous structural solid is used.

The element has three degree of freedom at each node; translation in the nodal X, Y, Z directions. The element is suitable for shape memory modeling case because it has large deflection, and large strain capabilities as shown in figure 3.8. Same dimension block of 10 mm (as in above test case) is used. The material properties and shape memory constants used in this simulation is given in table 3.2. The result of loading and unloading the block is shown in figure 3.9 for the temperature 285.15 K and for temperature 253.15 K the result of stress in respect of strain is shown in figure 3.10. As can be seen, the transformation strain in loading is generated, and strain has been recovered during the unloading. The corresponding Ansys script for the simulation of shape memory is listed in Appendix. This simulation showed the ability of the numerical tool in modeling the shape memory effect behavior of shape memory alloy materials.

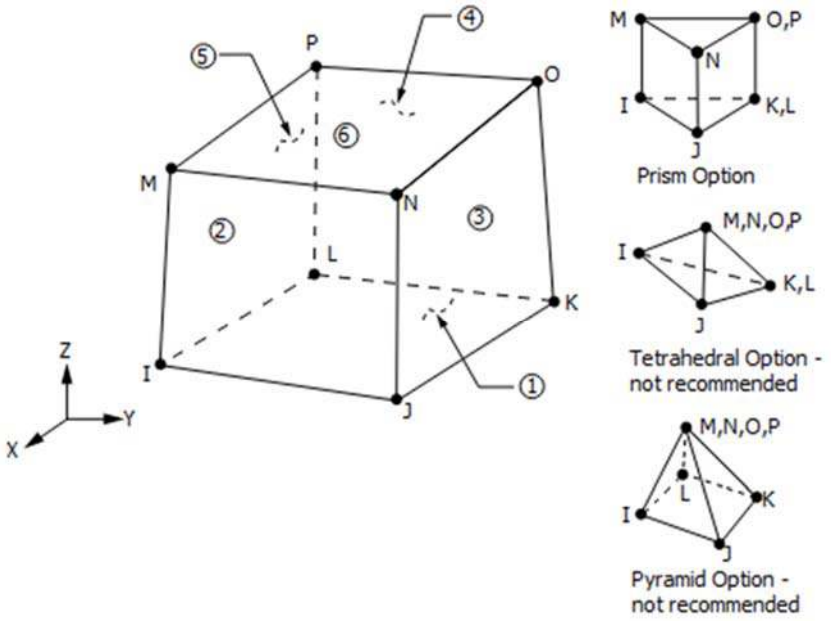

Figure 3.8: Schematic illustration of element type (SOLID185)

Table 3.2: Material properties of shape memory alloy used in preliminary simulations for shape memory test case.

Shape memory alloy Constants	Abbreviation	Value
Hardening parameter	h	500 MPa
Reference temperature	T_0	253.15 K
Elastic limit	R	45 MPa
Temperature scaling parameter	σ_f^{SA}	7.5 MPa
Maximum transformation strain	$\overline{\varepsilon_L}$	0.03
Martensite modulus	E_m	$70E^3$
Lode dependency parameter	m	0
Material Properties	**Abbreviation**	**Value**
Elastic modulus (Austenite phase)	E_A	70×10^3 MPa
Poisson Ratio	μ	0.33

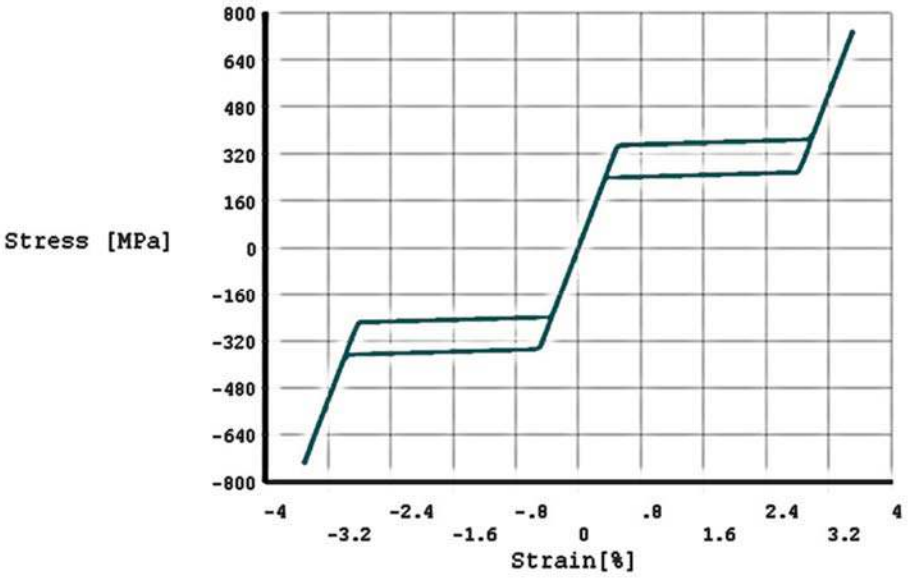

Figure 3.9: Preliminary output of simulation of shape memory behavior of Nitinol at temperature 285.15 K

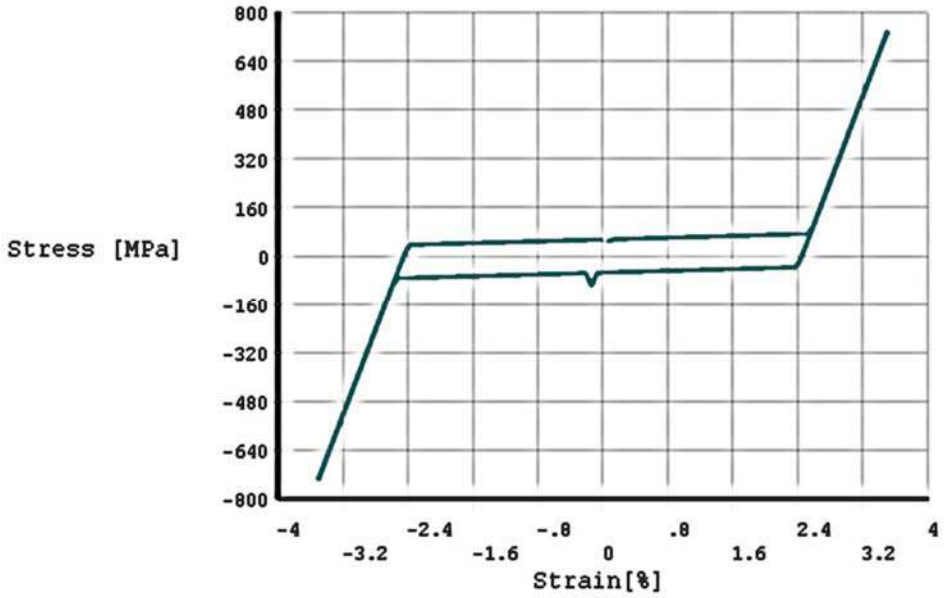

Figure 3.10: Preliminary output of simulation of shape memory behavior of Nitinol at temperature 253.15 K.

The nonlinearity and formation of transformation strains in both negative and positive directions can be clearly seen from this figure 3.9 and 3.10. The residual strain after unloading from the block is recovered by raising the temperature up to A_f whereas the formation of detwinned Martensite does not incur any shape change as predicted.

3.5 Validation of the numerical tool

To be able to use the developed numerical tool in Ansys to analyze shape memory alloys thermo-mechanical behavior, the generated output results should be verified against some experimental results. To this end, in the following sections, the numerical tool's results are compared with experimental results published in literature.

3.5.1 Validation for superelastic test case

To validate the numerical tool in Ansys and modeling shape memory alloy material behavior in superelastic case, the model was confirmed in tension against a previously published experiment. For all simulations presented, implicit Ansys solver was utilized. The tensile simulations match the experimental tensile test plot performed by Auricchio et al. (Auricchio et al., 1997) as shown in Table 3.3

Table 3.3: Comparison of numerical tool for superelastic test case with the experimental data published in literature

SUPERELASTIC TEST VALIDATION OF 2D CASE			
	Experimental	**Ansys Solver**	**Ratio**
σ_s^{AS}	520.00	522.013	1.004
ε_s^{AS}	0.010	0.010	1.046
σ_f^{AS}	600.00	599.992	1.000
ε_f^{AS}	0.080	0.08	1.000
σ_s^{SA}	300.00	300.016	1.000
ε_s^{SA}	0.074	0.075	1.013
σ_f^{SA}	200.00	197.500	0.988
ε_f^{SA}	0.003	0.003	1.029
SUPERELASTIC TEST VALIDATION OF 3D CASE			
	Experimental	**Ansys Solver**	**Ratio**
σ_s^{AS}	520.00	522.007	1.004
ε_s^{AS}	0.010	0.010	1.046
σ_f^{AS}	600.00	599.996	1.000
ε_f^{AS}	0.080	0.08	1.000
σ_s^{SA}	300.00	300.0086	1.000
ε_s^{SA}	0.074	0.075	1.013
σ_f^{SA}	200.00	197.689	0.988
ε_f^{SA}	0.003	0.003	1.029

3.5.2 Validation of the shape memory test case

To validate the combination of the Ansys solver and the developed numerical tool in modeling shape memory effect in temperature of 285.15 K and 253.15 K, the results of the simulation were compared to the experimental data published by Auricchio et al., in 2002. The compared values are given in table 3.4.

Table 3.4: Comparison of numerical tool for shape memory test case with the experimental data published in literature

SHAPE MEMORY CASE TEST VALIDATION AT TEMPERATURE 285.15 K			
	Experimental	**Ansys Solver**	**Ratio**
σ_s^{AS}	345.0	349.508	1.013
σ_f^{AS}	367.0	367.168	1.000
σ_s^{SA}	258.0	257.071	0.996
σ_f^{SA}	236.0	238.891	1.012
SHAPE MEMORY CASE TEST VALIDATION AT TEMPERATURE 253.15 K			
	Experimental	**Ansys Solver**	**Ratio**
σ_s^{AS}	54.6	55.568	1.018
σ_f^{AS}	74.1	73.229	0.988
σ_s^{SA}	-37.1	-36.868	0.994

These validation of the developed numerical tool with published experimental data in literature shows the higher accuracy of this tool. It is proved that we can further proceed for complex designs which uses shape memory alloys.

3.6 Finite Element Simulation of the novel acetabular screw

Acetabular screws, which are used as an anchoring point for implanting acetabular components (metal cup) in the THR and deformity treatments, entail a major drawback i.e.

loosening and back-out in the osteoporotic bone. The strength of the screw contact with the surrounding bone diminishes as the bone degrades e.g. due to osteoporosis.

A novel acetabular screw design is developed to address this issue which uses nitinol superelastic-shape memory elements (thread insert) wrapped around it. The smart assembly consists of an external superelastic tube which is responsible for expanding the design protrusions when reached to body temperature; also an internal shape memory wire, inserted into the tube, is sought to retract the assembly while locally heated to above the body temperature (Refer to chapter 2 for more details). The whole assembly can be evaluated and optimized as for the interaction of the superelastic tube and shape memory wire using the model developed in Ansys mechanical.

3.6.1 Delineation and linearization of the problem

Bone screws have been used in THR since the 1990s, when the modular cup are proposed with holes. Acetabular screw is a particular type of bone screw designed for enhancing the fixation of acetabular cups. The acetabular screw provides a means of gripping a pelvic segment. One major drawback in THR procedure using acetabular screws is due to the adverse effects of osteoporosis. Osteoporotic bone, because of the degradation of the supporting bone structures, cannot provide enough anchoring foundation for the screw to be implanted into; therefore, acetabular screw placement in the osteoporotic bone involves the risk of intra-operation or post-operation screw pull-out/loosening. One proposed solution to enhance the performance of the acetabular screws in the osteoporotic bone utilizes shape memory-pseudoelastic nitinol antagonistic beam assembly.

The linearized prototype of the novel acetabular screw consists of a base screw and a few assemblies of SMA wire and tube. The base screw is similar to the traditional acetabular screws except for an additional circular thread cut on the minor surface as well as transverse.

The SMA wire-tube assembly will be inserted and fixated into these holes. The wire should activate at above body temperature and it should be in Martensite phase when in body temperature. The tube, made of another composition of nitinol has an activation temperature around body temperature. The wire should be inserted into the tube. Then the assembly of wire and tube is wrapped around the base screw and fitted in the circular cut on the surface of the screw. The stem of the wire-tube assembly is welded to the screw for achieving better fixation. The assembly of the wire and tube is depicted in Figure 3.11.

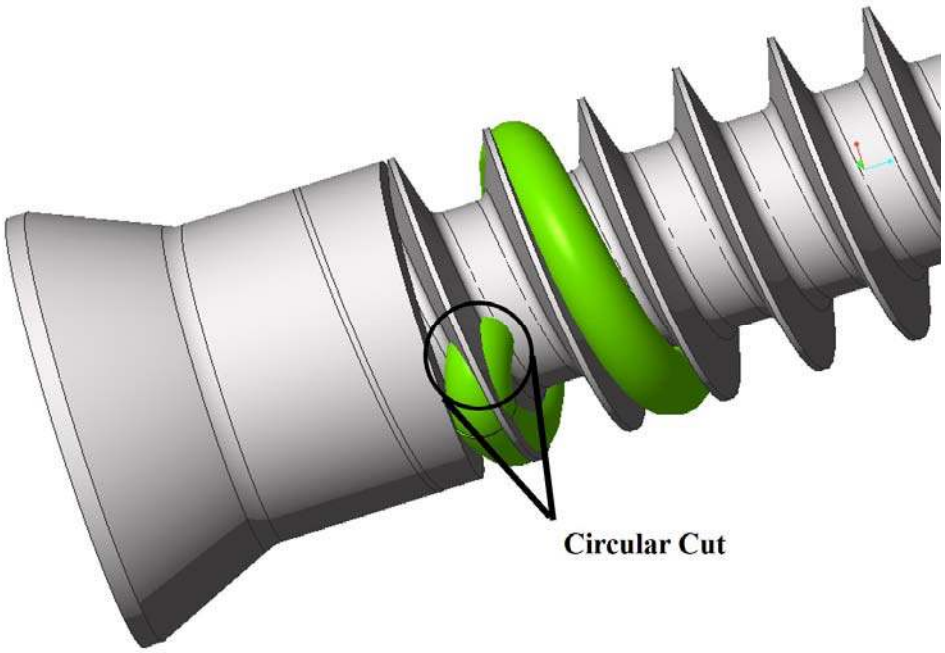

Figure 3.11: The SMA helical insert is fused to the holes on the surface of the screw.

3.6.2 Contrasting shape memory-pseudoelastic beam assembly

The assembly consists of a pseudoelastic nitinol (with lower A_f temperature) tubular beam and a shape memory nitinol (with higher A_f temperature) circular beam; as illustrated in figure 3.12. Moreover, according to figure 3.13, the initial memorized shapes of both the tube and the wire are bent off the centerline in opposite directions.

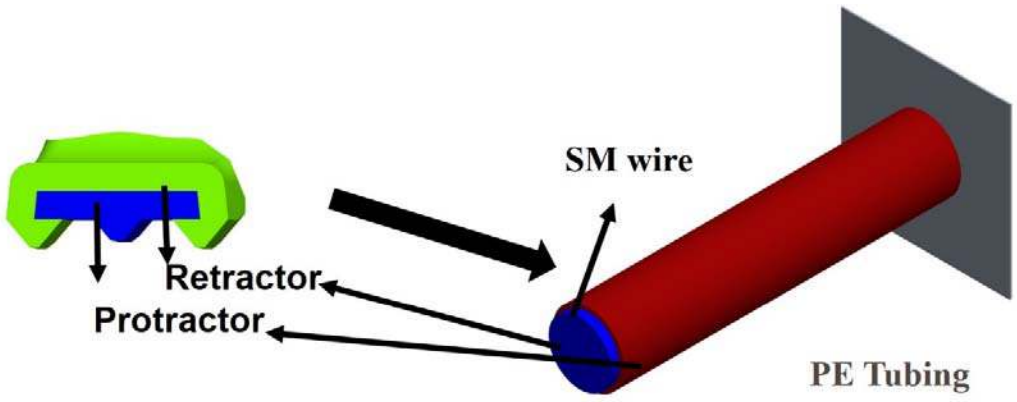

Figure 3.12: Linearized insert elements assembly to circular tubing and beam assembly.

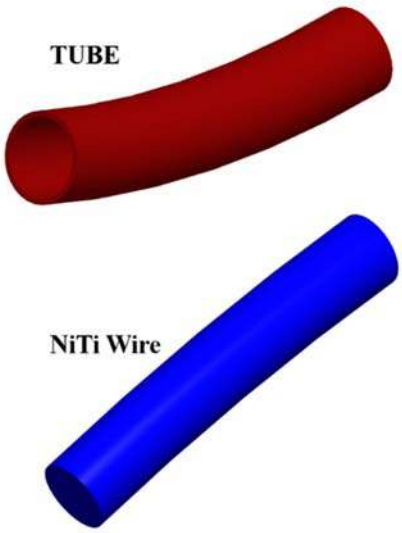

Figure 3.13: Initial memorized shapes of the nitinol wire and tube assembly.

The basis of operation is the difference in the transformation temperatures between the wire and the tube. At a so-called low temperature (body temperature 37°C for the present biomedical purpose), the tube is superelastic and the wire is shape memory. On the other hand, at a higher temperature level (suppose 52°C) the wire also becomes superelastic. Beyond this level of temperature, both the wire and the tube exist in Austenite state, at which their memorized shape is stable. This process is depicted in figure 3.14. Suppose the operation process begins from a very low temperature at which the assembly resides in a straight state; deformed compared to the memorized shapes. By reaching the lower temperature level as the second stage, the tube will transform to the stiffer Austenite form while the wire will remain in the flexible Martensite form; hence the tube tends to raise the assembly upwards towards its memorized situation. The third stage is to heat the assembly to the high temperature level. By that point, the wire also will have become Austenite and have acted against the current situation, pushing the assembly down.

Functioning of the smart acetabular screw requires that the amount by which the assembly moves upwards at body temperature (Figure 3.14-B) to be large. In addition, the amount of bending downwards at high temperature (Figure 3.14-C) should be such that the assembly gets back as much as possible to the zero straight condition (Figure 3.14-A).

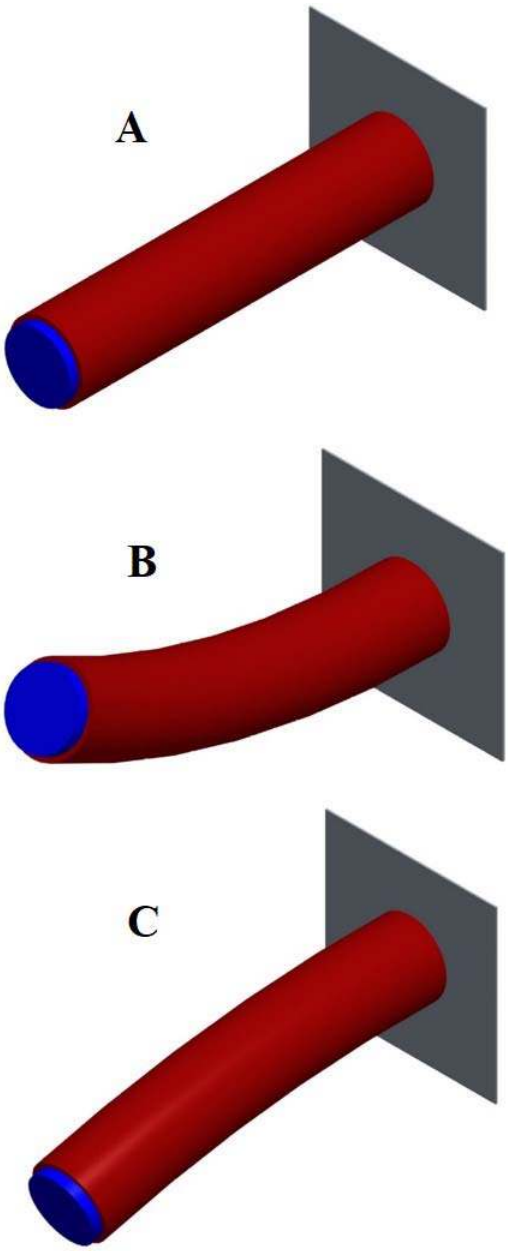

Figure 3.14: Assembly at (A) the straight condition (at the time of surgery) (B) Desired low temperature form (37°C) after activation of the tube: the assembly is bent upwards (at the time when bone degrades) (b) Desired high temperature form (52°C) after activation of the wire: the assembly is re-bent downwards (removing screw for any reason)

3.6.3 FE simulation results and discussion

It was shown in chapter 2, that the design of the smart acetabular screw can approximately be modeled as an assembly of a wire and a tube. The model consists of a wire which has a circular deformation upwards and a tube which has a circular deformation downwards (Figure 13). With this configuration, the assembly after engagement can assume three different deflection modes. One is at a relatively low temperature where both the wire and the tube are in the Martensite state. It is possible to engage the wire into the tube at this situation and fixate the assembly to the body of the novel screw. Figure 3.15 shows the model of the wire and the tube in the original configuration. The straight dashed line represents the surface of the screw. This is a situation where the SMA protrusions are in the collapsed form at the time of implanting the screw in the bone. Secondly, at a temperature around 37°C (body temperature), the tube will transform into Austenite state and tend to bend the whole assembly in favor of its initial deformed state. This represents the situation where the SMA protrusions of the smart screw are expanded. Finally, the third configuration is reached at a temperature above 52°C. It is the retraction condition for the SMA protrusion at the time of removing the screw. The smart screw can be removed or revised by heating it up to the A_f of the retractor wires. In that case, the wire activates and tends to deflect the assembly back to the collapsed condition. The operation stages are summarized in Figure 3.15.

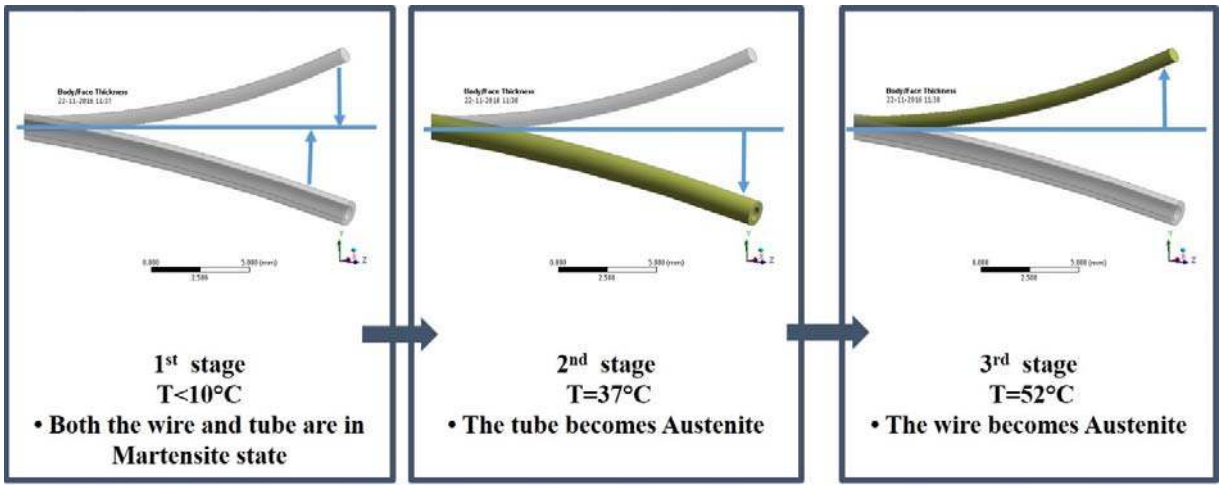

Figure 3.15: Different stages of the wire-tube assembly operation.

This assembly is transferred to Ansys workbench to be simulated via the SMA capability developed in the framework of this software. Figure 3.16 shows the meshing of the assembly with quadratic hexahedral elements. The model consists of a total of 41889 elements and 10650 nodes.

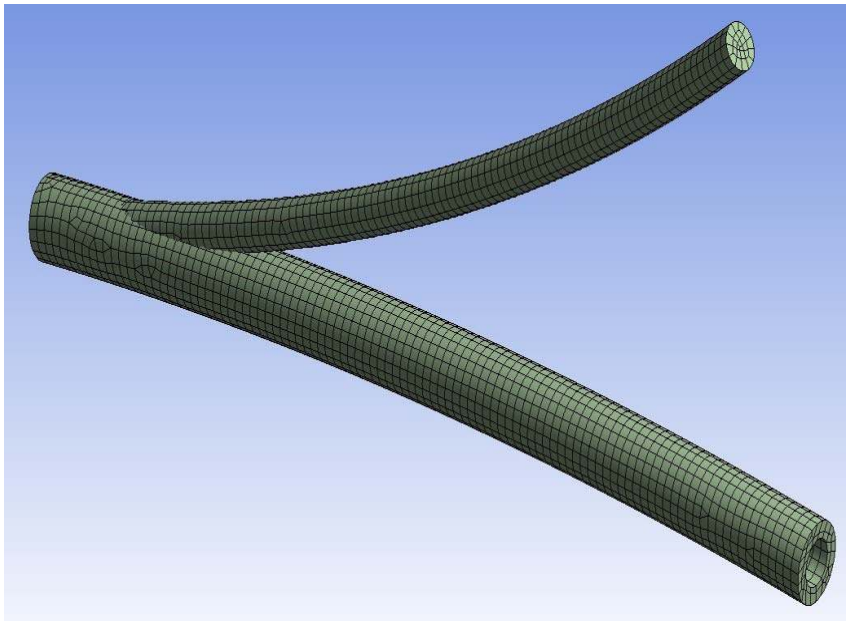

Figure 3.16: Discretization of wire tube assembly with SOLID185 (3D 8-Node Structural Solid) with large deformation effect enabled.

Furthermore, the variation of temperature at different stages of the simulation is shown in Figure 3.17. For further simplicity and in order to avoid complications of contact modeling, the following approach in modeling is adopted. The wire and the tube are deformed at the 1st stage temperature level under a distributed tip loading. The loading causes Martensite transformation in top and bottom layers of the tube and wire that sustain the highest amount of stress. Therefore, upon unloading, there will be some residual deformation in the structure. The type of loading and boundary conditions (B.C.) used for this model are shown in figure 3.18. Loading wire (L1) = 0 to -1.6 N and tube of tube (L2) = 0 to +16N is applied. In this case, a symmetry B.C. is considered at the end of the cantilever tube and wire for achieving a better convergence.

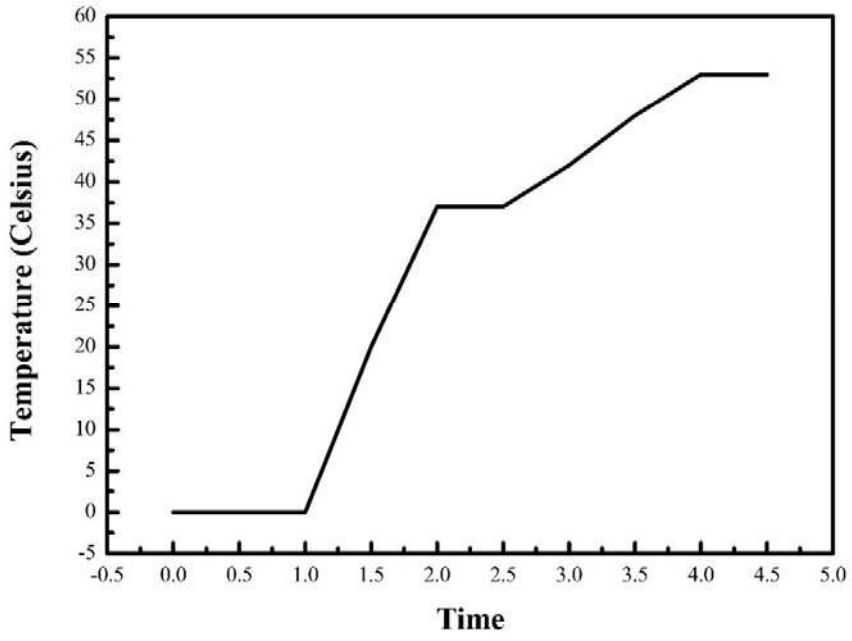

Figure 3.17: Variation of temperature at 1st, 2nd and 3rd stage.

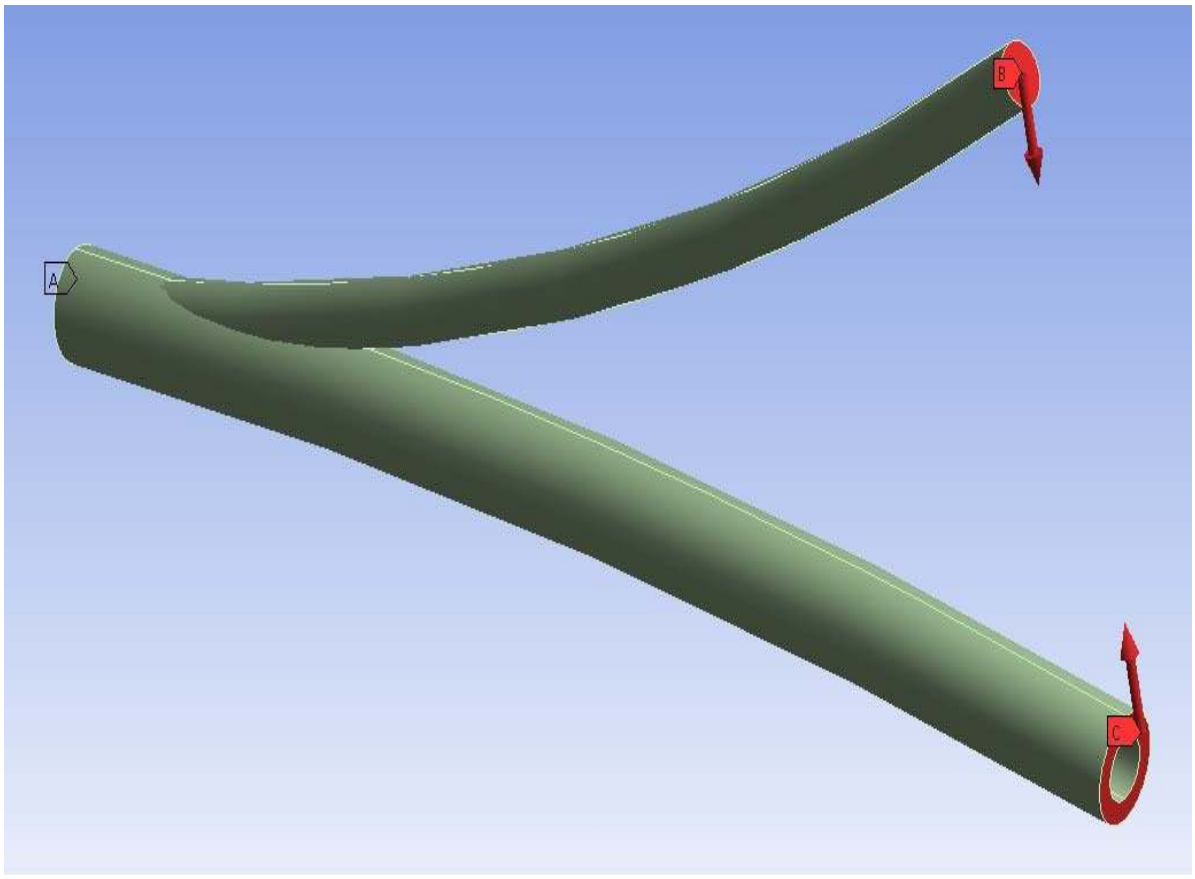

Figure 3.18: Loading and boundary condition of nitinol wire tube assembly.

The typical distribution of detwinned Martensite in the wire-tube assembly is illustrated in Figure 3.19. The figure belongs to a solution instance at the second stage (See Figure 3.15) and shows the consumption of detwinned Martensite in transformation to stress-induced Martensite at the layers of the beams with higher stress levels.

The load-deflection plots for the wire and tube at the low temperature level (first stage) are depicted in figure 3.20 and figure 3.21. As mentioned earlier, both the wire and tube are loaded from 100% detwinned Martensite and retain the transformation strain after unloading.

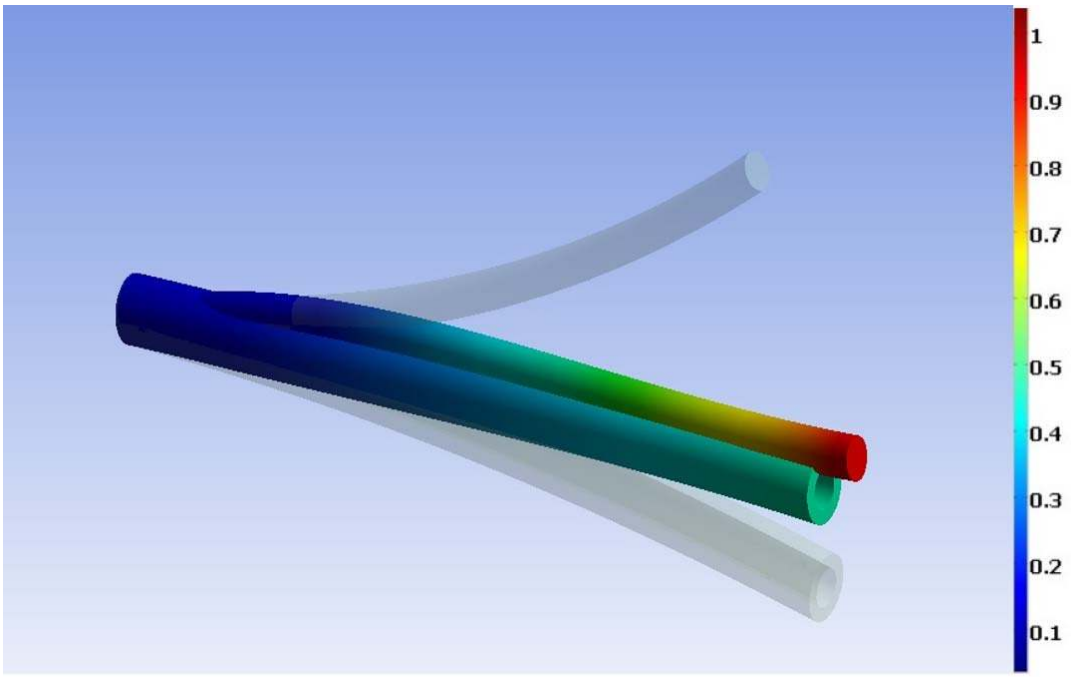

Figure 3.19: Typical Martensite distribution in the assembly (ζ_d shown here).

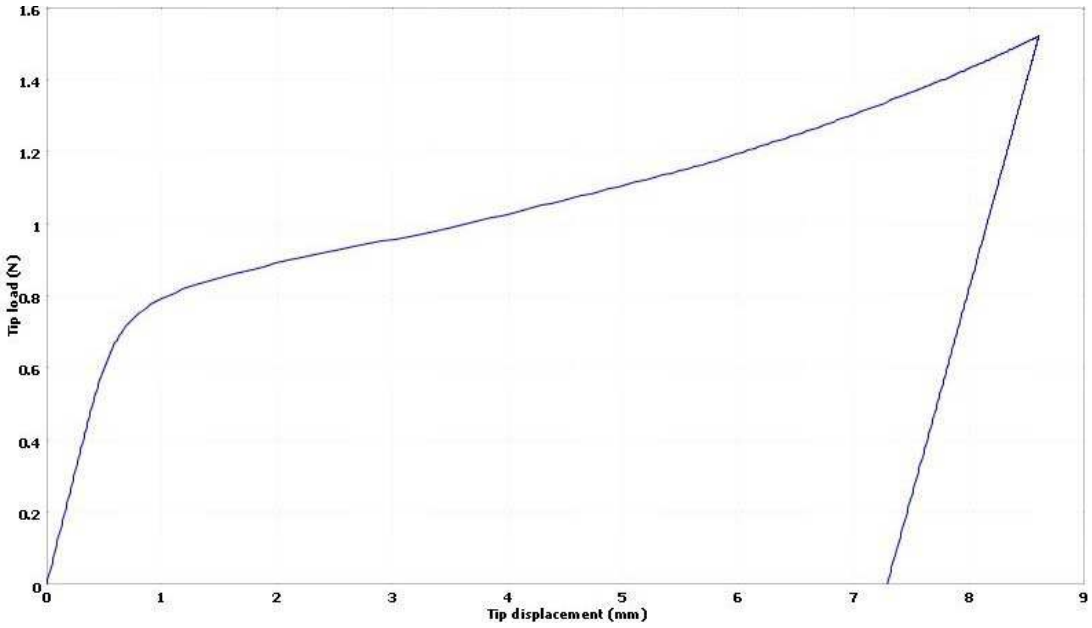

Figure 3.20: The deflection of the wire under a tip load at the first stage (1st stage).

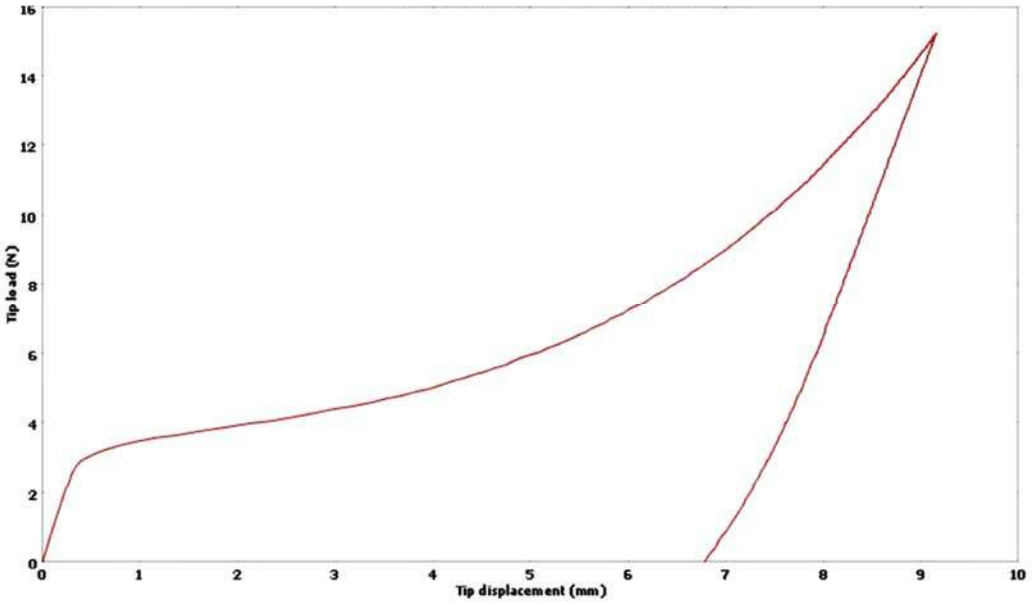

Figure 3.21: The deflection of the tube under a tip load at the first stage (1st stage).

The state of equilibrium is noted in Figure 3.22 where the sum of the deflections of the wire and the tube at the tip under a load of 1.2 N equals the initial gap. The initial gap between the wire and the tube at the tip is $\{H1 + H2 = 2.44 + 3.26 = 5.7\ mm\}$ (Figure 3.23).

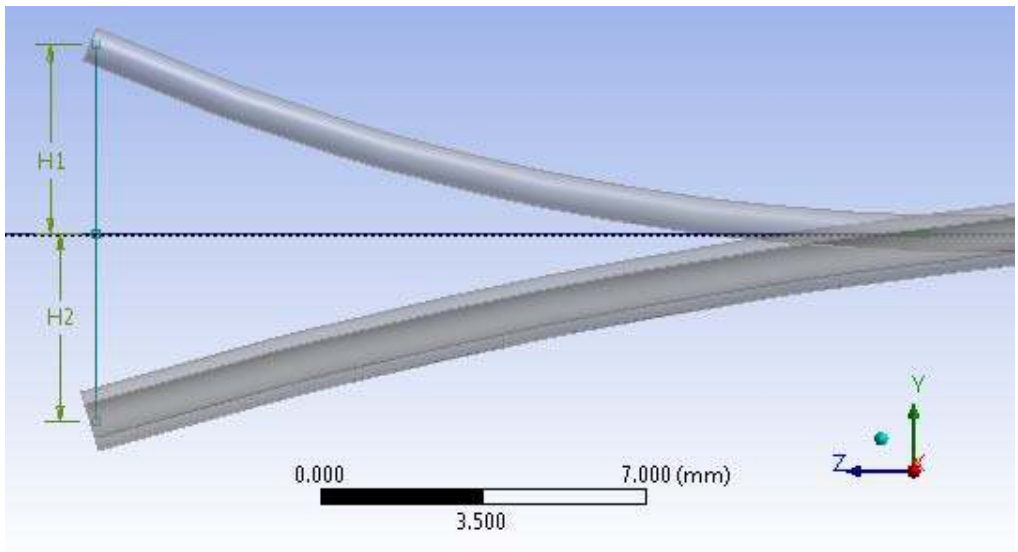

Figure 3.22: Illustration of state of equilibrium

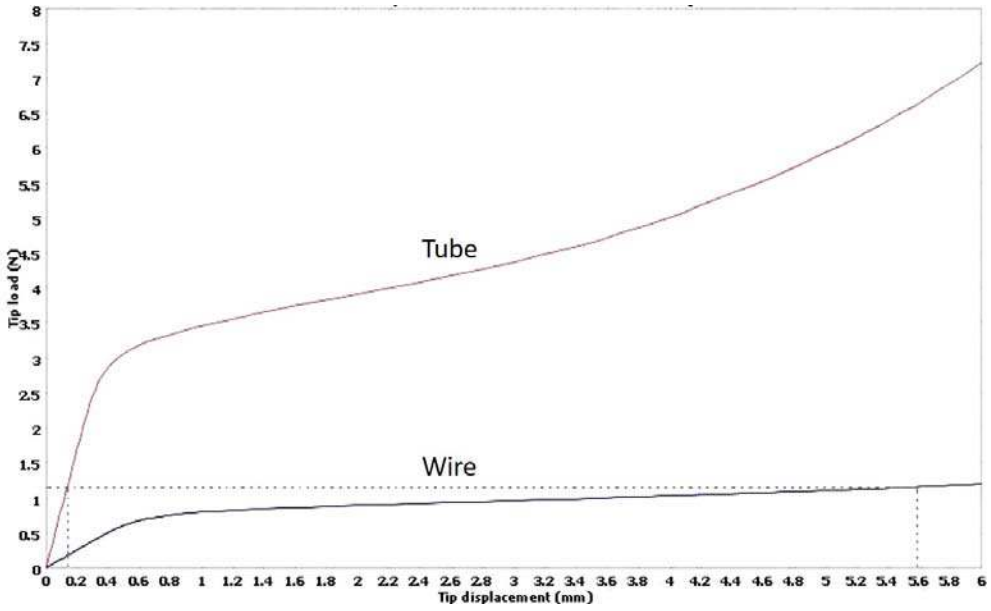

Figure 3.23: Load-displacement plots for the wire-tube assembly at the first stage.

Figure 3.24 and Figure 3.25 show the deflection behavior at the second stage. While the system is at body temperature, the tube transforms to Austenite state which is a stiffer and stronger phase than Martensite. Therefore, the behavior of the tube denotes a closed hysteresis. Load displacement plot for witre and tube is shown in figure 3.26

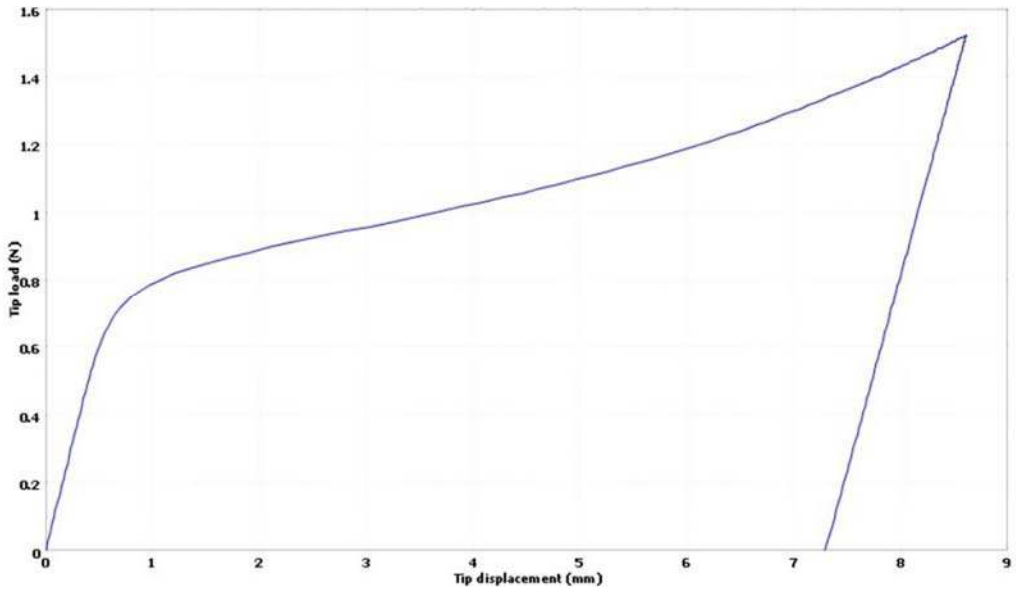

Figure 3.24: The load-deflection for wire at body temperature (2nd Stage)

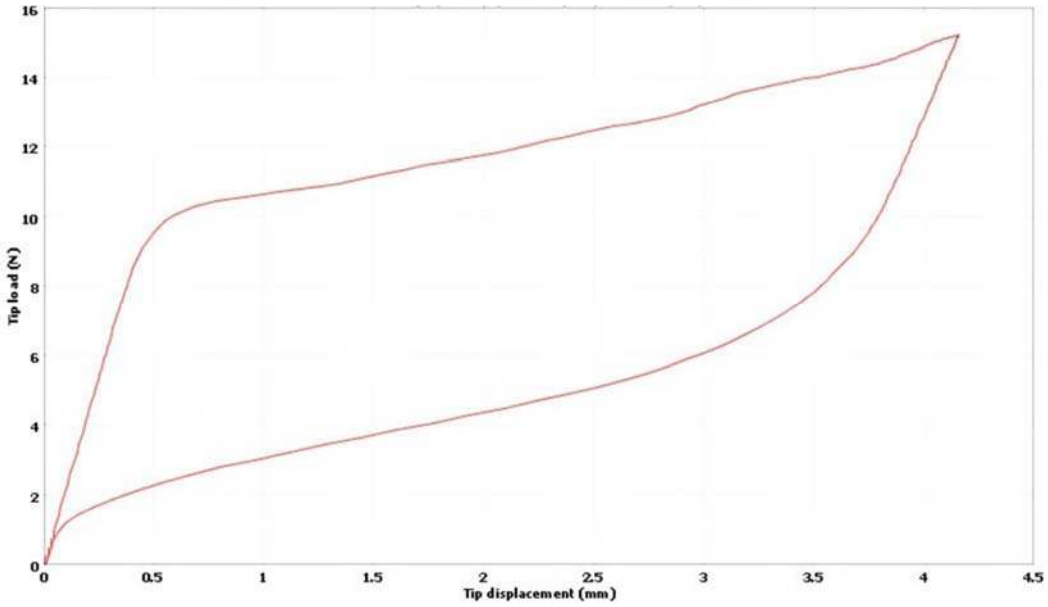

Figure 3.25: The load-deflection for tube at body temperature (2nd Stage)

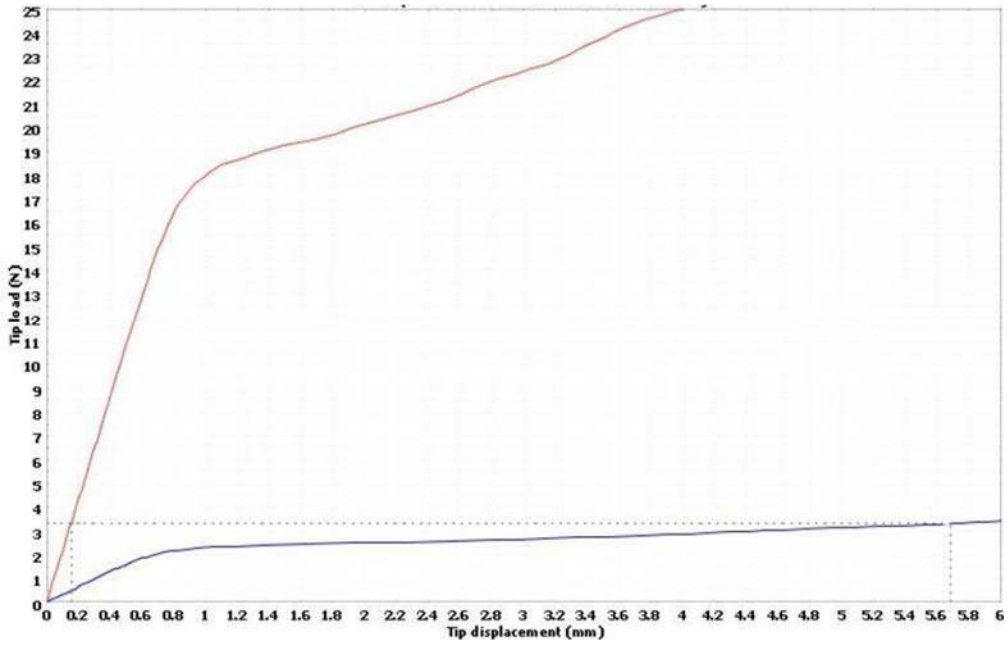

Figure 3.26: Load-displacement plots for the wire-tube assembly at the 2nd stage

Finally, the load displacement plots for the third stage are brought in figure 3.27 and Figure 3.28. Tip load and tip displacement of wire and tube is shown in figure 3.29. Because both the wire and the tube are in the Austenitic phase at this level of temperature, they show

pseudoelastic hysteresis in their deflection behavior.

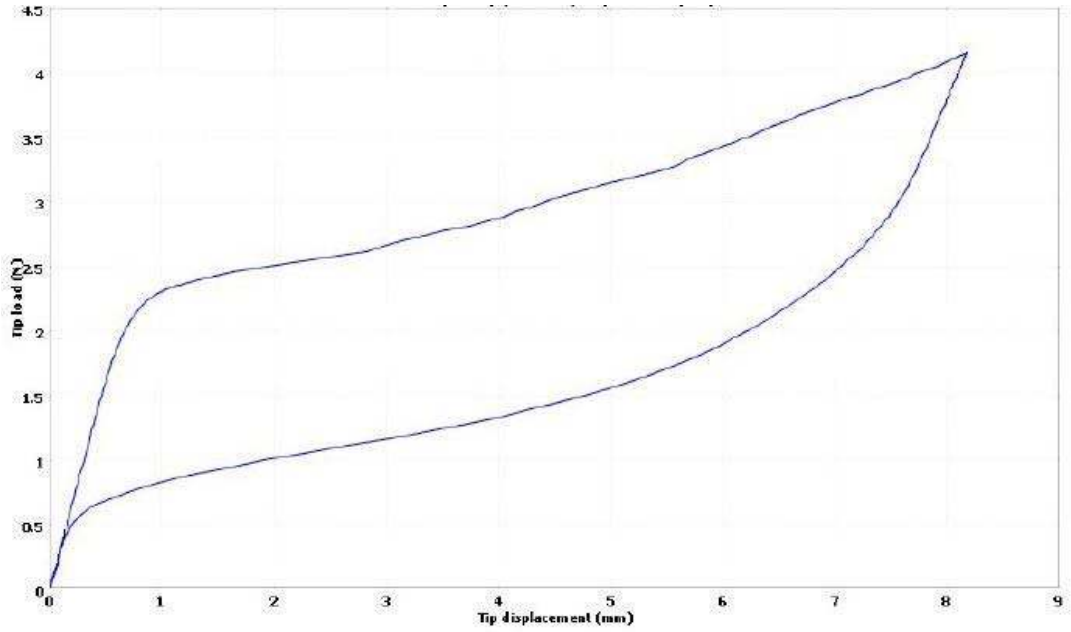

Figure 3.27: The deflection of the wire under a tip load at the 3rd stage.

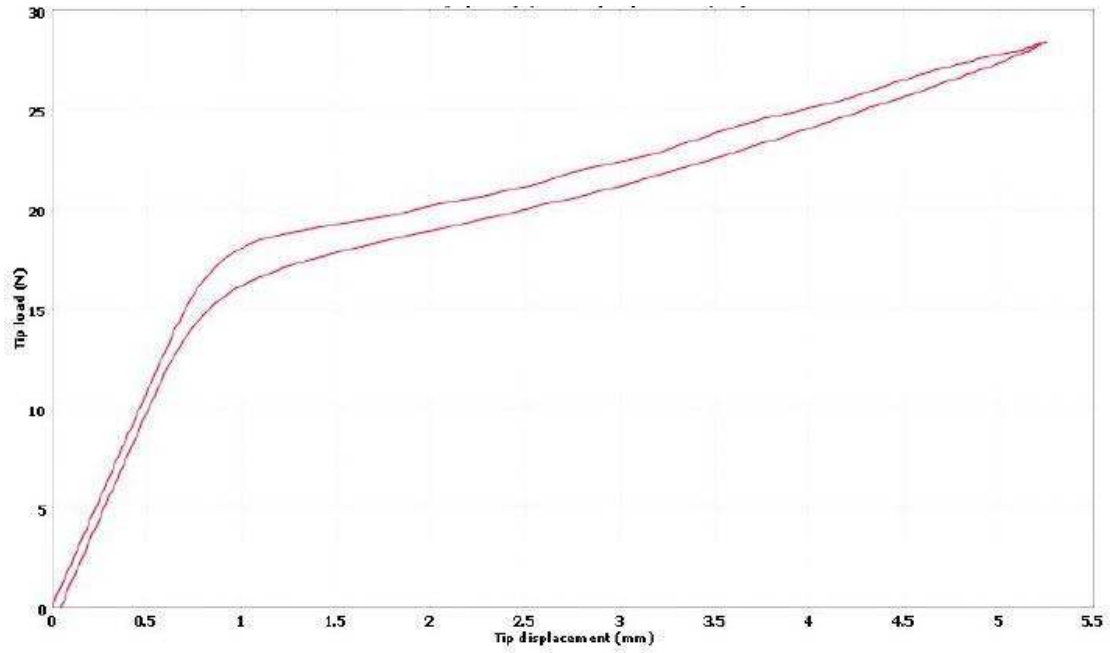

Figure 3.28: The deflection of the tube under a tip load at the 3rd stage.

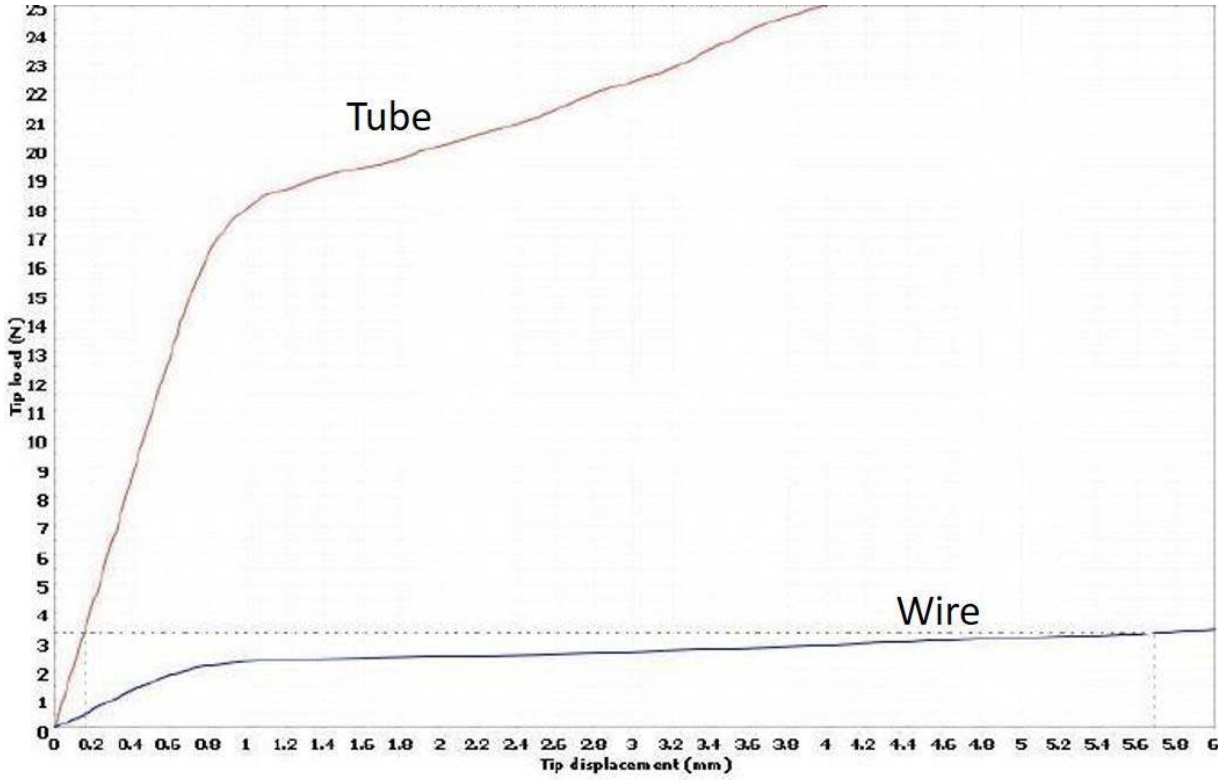

Figure 3.29: Load-displacement plots for the wire-tube assembly at the 3rd stage.

In respect to the design point of nitinol components is the strain the material sustains. If the application entails cyclic loading, the strain should not surpass 3% to keep the fatigue properties of nitinol in a safe margin. The current application is a one-time operating one, although fatigue external loadings might act upon the screw. Figure 3.30 illustrates the first principle strain plots of the wire and the tube at the instance of their maximum deformation. The 8 % maximum level, which pertains to the superelastic tube, is in the normal operating range for nitinol alloys.

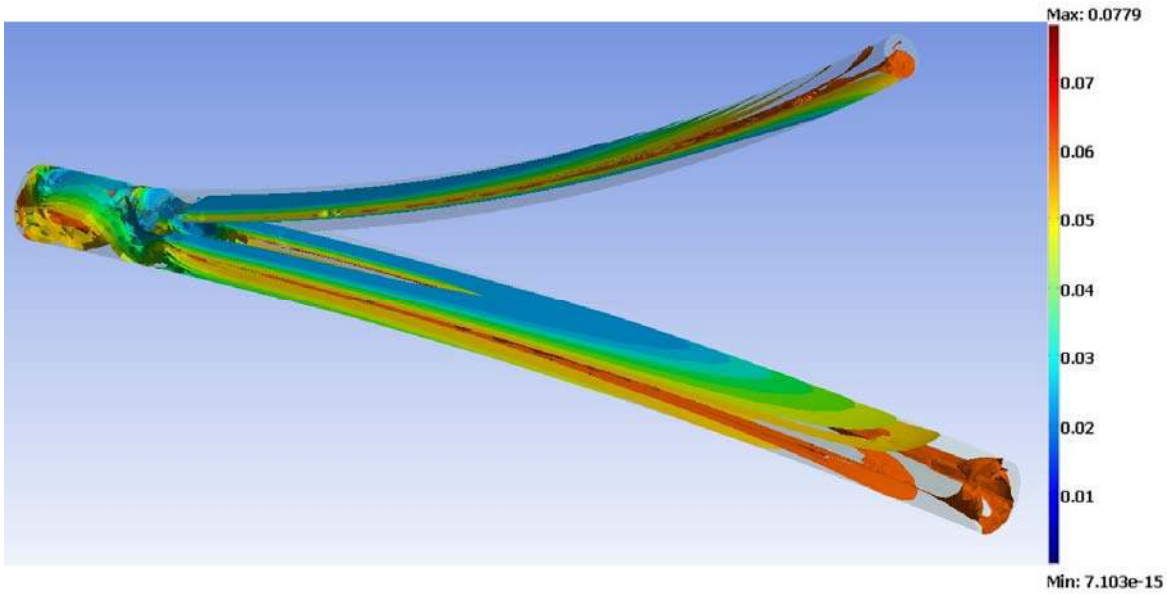

Figure 3.30: First principle strain of wire-tube at the instance of their maximum deformation (8% max. to superelastic tube)

3.7 Pilot testing of the novel Acetabular screw

Performance of the novel acetabular screw was tested in the course of a pilot pull out experiment. Standard hex head lag stainless steel screw of the length 5 ¾ and ¼ thread size were taken and assembled with nitinol wires. Head of the screw is cut down to achieve a proper grip with fixture. A long nitinol wires with a diameter of 0.7 mm was braked down into pieces of 20 mm. The screw was cross drilled to prepare hole of 0.7 mm to fix these nitinol wire pieces. These holes were drilled in such a pattern that there beginning and end would be on different levels of the thread by keeping in mind so as thread must not be damaged (Figure 3.31). The both ends of wires were closed at the time of screw insertion and reopens when placed into the material. The screw assembled with nitinol is inserted into a cellular rigid polyurethane foam block of dimension 43×43×90 mm with the density of 12.5 lb/ft3 (0.20 g/cc).

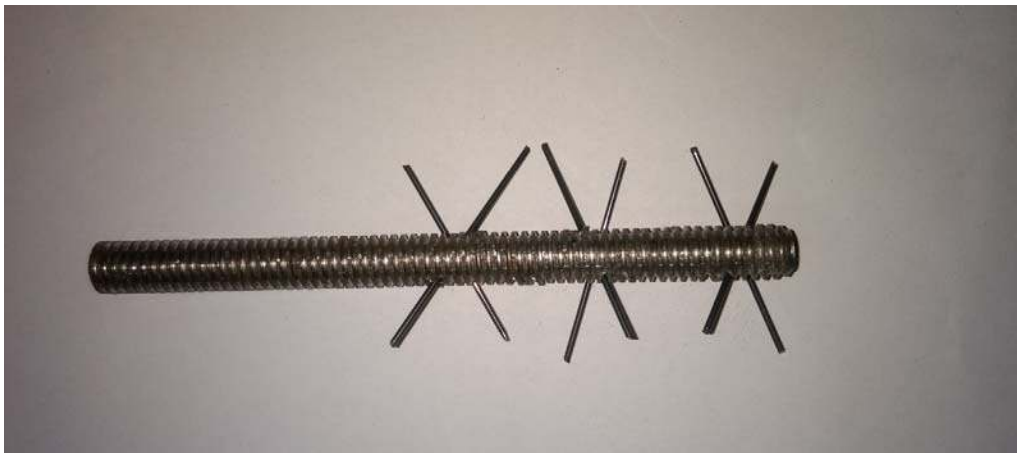

Figure 3.31: Screw assembled with nitinol wires

This density of polyurethane foam block is comparable with normal human bone. This setup was used to make the test of axial pull out strength of screws performance.

Prior to insertion, a hole was drilled and tapped into the block with a diameter of ¼. The size of the whole was selected a little larger with respect to the thread size of the lag screw in order to represent osteoporotic bone. The primary objective of the design of the bone screw enhanced with nitinol wires is to overcome this drawback by further opening the wires which could maintain the contact with the receded bone. The screw insertion depth in the foam block was 53 mm. A control specimen was also prepared with exact same specifications but using an original lag screw. The specimens were evaluated on a testing machine with a tensile pull-out load applied to the head of the screws; as illustrated in Figure 3.32. The pulling rate was set to 5 mm/min in accordance with ASTM F543 - 17. The results are depicted in Figure 33 as tensile load versus displacement graphs.

Figure 3.32: Experimental setup for measuring pull out strength of screw; setup shows the screw is inserted in the cellular rigid polyurethane foam block and fixed on the UTM.

The mode of failure was rupturing of the material surrounding the screw thread. The load at the instance where the displacement reached equal to the screw pitch was chosen as the strengths of the screw. The improvement in the pull-out strength of the screw via enhancing

it with superelastic SMA wires is obvious from this figure. It is worth noting that novel screw would gain resistance again after the displacement reached which can be attributed to the repeated entanglement of the nitinol wires with the foam resulting in further resistance of the screw against the pull-out force; a behavior which could not be seen in the control specimen. The outcomes of this experiment would demonstrate the effectiveness of the novel screw design.

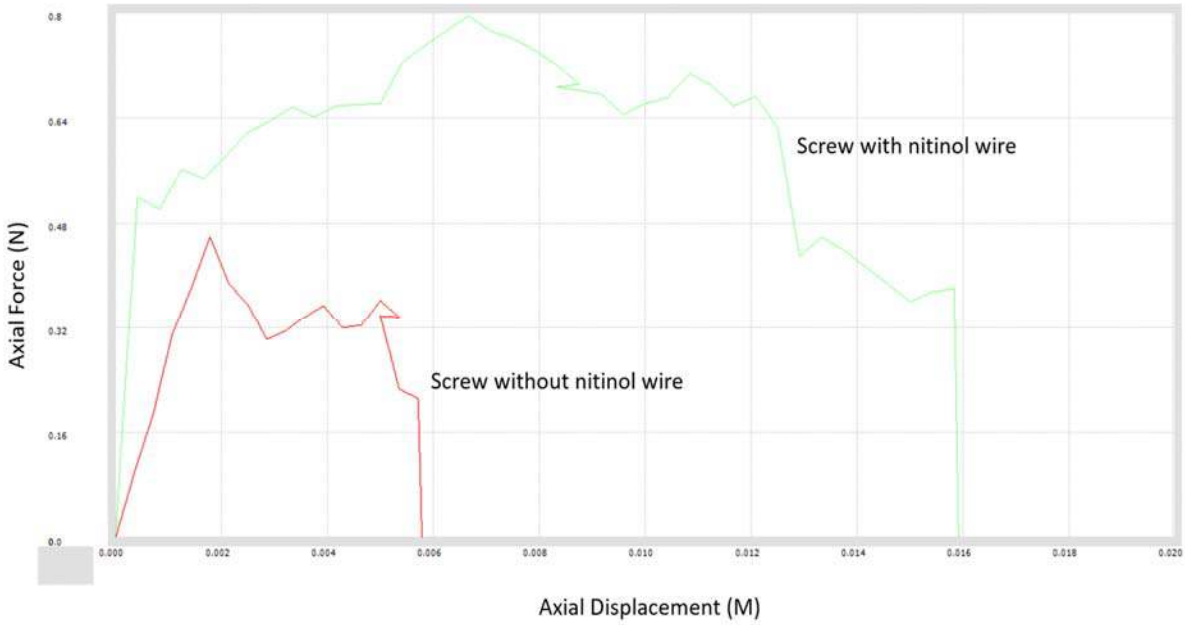

Figure 3.33: Results of the axial tensile test: force versus displacement. The tensile strength is selected at the force required to displace the screw in the block as much as the screw thread pitch.

3.8 Predicting outcomes of novel press-fit acetabular cup design

Based on the above FE simulations and pilot experiment of the novel screw anchored with nitinol elements, it is evident that implementing nitinol in rig will surely give the enhanced

pullout strength of the acetabular screw rather than the conventional press-fit acetabular cup.

3.9 Conclusion

Shape memory alloys are a unique kind of alloys which show a specific thermo-mechanical behavior. They have the ability to return to a certain predefined shape upon heating after deformation. The second specific property is the ability to tolerate large deformations without undergoing the plastic region. These specific properties along with the biocompatibility of nitinol are the reasons that this alloy has been used in recent years for biomedical devices applications

To better design and analyze the nitinol devices which are used in biomedical applications, a simulation tool is required. To this end, the constitutive modeling of the thermo-mechanical behavior of the shape memory alloys has been implemented into the Ansys solver.

A novel total hip implant design which has been proposed and analyzed in this study. The unique part of the design was the nitinol assemblies which were placed on the acetabular cup and screw. The assemblies were made out of nitinol material which brought the capability of expanding and retracting (in certain temperatures) to the screw. The functionality of the described assembly was evaluated by making a prototype in larger scale and performing experiments. The result of the tip displacement of the assembly was recorded and reported as the function of temperature variation of the nitinol beam. The FE modeling of nitinol thermo-mechanical behavior in Ansys was also conducted and verified

by comparing the results with the experimental ones. Pullout test as the standard method of evaluating the acetabular screws was also modeled in Ansys as the FEA modeling software. In the experiment, the pullout test results of a regular screw were compared to the enhanced screw with nitinol wires. In both experiment and modeling, the screw with nitinol showed much higher pullout force than a regular screw.

3.10 Future work

This work can be continued in different aspects. First, the numerical thermo-mechanical modeling of the shape memory alloy material in Ansys can be further improved. Shape memory alloys are known to have different behaviors in different rates of loading the material. The numerical model can be developed to capture the rate dependency of the shape memory alloy behaviors based on the developed equations in literature. This capability enables the numerical tool to be able to be used in variety of applications. possibility to modify, analyze and prototype other designs for the acetabular screw to better mitigate osteoporosis effect. In the future designs, the possibility of easy production of the device should be better considered. In the design procedure different capabilities in producing nitinol geometries should be considered.

Additionally, the pullout test finite element simulation can be performed in more realistic way and be compared to the experiments. The procedure of failure of the bone in the pullout test of acetabular screw should be studied in more medical aspects details and be considered in the modeling. After the production of a novel acetabular screw the pullout tests in a bone material can be performed and be compared to the result of a regular screw pullout test.